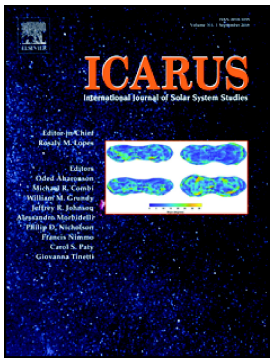

Spatiotemporal evolution, mineralogical composition, and transport mechanisms of long-runout landslides in Valles Marineris, Mars

Jessica A. Watkins, Bethany L. Ehlmann, An Yin

PII: S0019-1035(20)30217-7

DOI: https://doi.org/10.1016/j.icarus.2020.113836

Reference: YICAR 113836

To appear in: *Icarus*

Received date: 26 April 2020

Accepted date: 29 April 2020

Please cite this article as: J.A. Watkins, B.L. Ehlmann and A. Yin, Spatiotemporal evolution, mineralogical composition, and transport mechanisms of long-runout landslides in Valles Marineris, Mars, *Icarus* (2020), https://doi.org/10.1016/j.icarus.2020.113836

Spatiotemporal evolution, mineralogical composition, and transport mechanisms of long-runout landslides in Valles Marineris, Mars

Jessica A. Watkins[a,b,] (jwatkins@caltech.edu), Bethany L. Ehlmann[b,c,*] (ehlmann@caltech.edu), and An Yin[a] (yin@epss.ucla.edu)

[a] *Department of Earth, Planetary, and Space Sciences and Institute of Planets and Exoplanets (iPLEX), University of California, Los Angeles, CA 90095-1567, USA*

[b] *Division of Geological and Planetary Sciences, California Institute of Technology, Pasadena, CA 91125, USA*

[c] *Jet Propulsion Laboratory, California Institute of Technology, Pasadena, CA 91109, USA*

* Corresponding Author

Submitted to: Icarus

Submission date: July 3, 2018 (minor updates 25 April 2020)

Key Words: Landslides; Morphology; Geological processes; Hydrated Minerals; Mars

ABSTRACT

Long-runout landslides with transport distances of >50 km are ubiquitous in Valles Marineris (VM), yet the transport mechanisms remain poorly understood. Four decades of studies reveal significant variation in landslide morphology and emplacement age, but how these variations are related to landslide transport mechanisms is not clear. In this study, we address this question by conducting systematic geological mapping and compositional analysis of VM long-runout landslides using high-resolution Mars Reconnaissance Orbiter imagery and spectral data. Our work shows that: (1) a two-zone morphological division (i.e., an inner zone characterized by rotated blocks and an outer zone expressed by a thin sheet with a nearly flat surface) characterizes all major VM landslides; (2) landslide mobility is broadly dependent on landslide mass; and (3) the maximum width of the outer zone and its transport distance are inversely related to the basal friction that was estimated from the surface slope angle of the outer zone. Our comprehensive Compact Reconnaissance Imaging Spectrometer for Mars (CRISM) compositional analysis indicates that hydrated silicates are common in landslide outer zones and nearby trough-floor deposits. Furthermore, outer zones containing hydrated minerals are sometimes associated with longer runout and increased lateral spreading compared to those without detectable hydrated minerals. Finally, with one exception we find that hydrated minerals are absent in the inner zones of the investigated VM landslides. These results as whole suggest that hydrated minerals may have contributed to the magnitude of lateral spreading and long-distance forward transport of major VM landslides.

1. Introduction

Enigmatic long-runout (> 50 km) landslides have sculpted the morphology of Valles Marineris (VM) on Mars over the past 3.5 billion years (Blasius et al., 1977; Lucchitta, 1979;

McEwen, 1989; Witbeck et al., 1991; Quantin et al., 2004a,b; Crosta et al., 2018) (**Fig. 1**). The VM equatorial trough system, which is ~4500-km long, up to 700-km wide, and ~7-km deep, lies along the crest of a regionally extensive highland commonly referred to as the Tharsis Rise (**Fig. 1**) (e.g., Yin, 2012a). The VM trough zone extends eastward from the Tharsis Montes and Syria Planum in the west and terminates at Eos Chasma of the northern lowlands in the east (**Fig. 1**). The Tharsis Rise accounts for approximately 25% of the surface area of Mars and is the youngest tectonic province on the planet. The opening of the VM troughs may have started in the Late Noachian (e.g., Dohm et al., 2009) and lasted as late as the Late Amazonian (Blasius et al., 1977; Schultz, 1998; Witbeck et al., 1991; Yin, 2012b).

Due to their exceptional exposure and nearly complete preservation of surface morphology, VM landslides have been intensely studied since they were first revealed by Mariner 9 and Viking images (e.g., Lucchitta, 1978; 1979; 1987; McEwen, 1989; Schultz, 2002; Harrison and Grimm, 2003; Quantin et al., 2004a,b; Soukhovitskaya and Manga, 2006; Lajeunesse et al., 2006; Bigot-Cormier and Montgomery, 2007; Lucas and Mangeney, 2007; Lucas et al., 2011; De Blasio, 2011; Brunetti et al., 2014; Watkins et al., 2015). Early investigations of long-runout VM landslides in low-resolution Viking images included comparative study of the surface morphology (Lucchitta 1978; 1979; 1987) and morphometric parameters (McEwen, 1989) relative to terrestrial analogs. The distribution of VM landslides was first established by Witbeck et al. (1991). Subsequent studies based on higher-resolution images indicate a wide range of emplacement ages (i.e., ~3.5 Gy to ~50 My, **see Fig. 1B**) (Quantin et al., 2004b) and focus on quantitative morphologic analysis (De Blasio, 2011; Quantin et al., 2004a; Brunetti et al., 2014; Soukhovitskaya and Manga, 2006; Watkins et al., 2015), multidimensional numerical modeling (Harrison and Grimm, 2003; Lucas et al., 2011), and physical analogue experiments (Lajeunesse

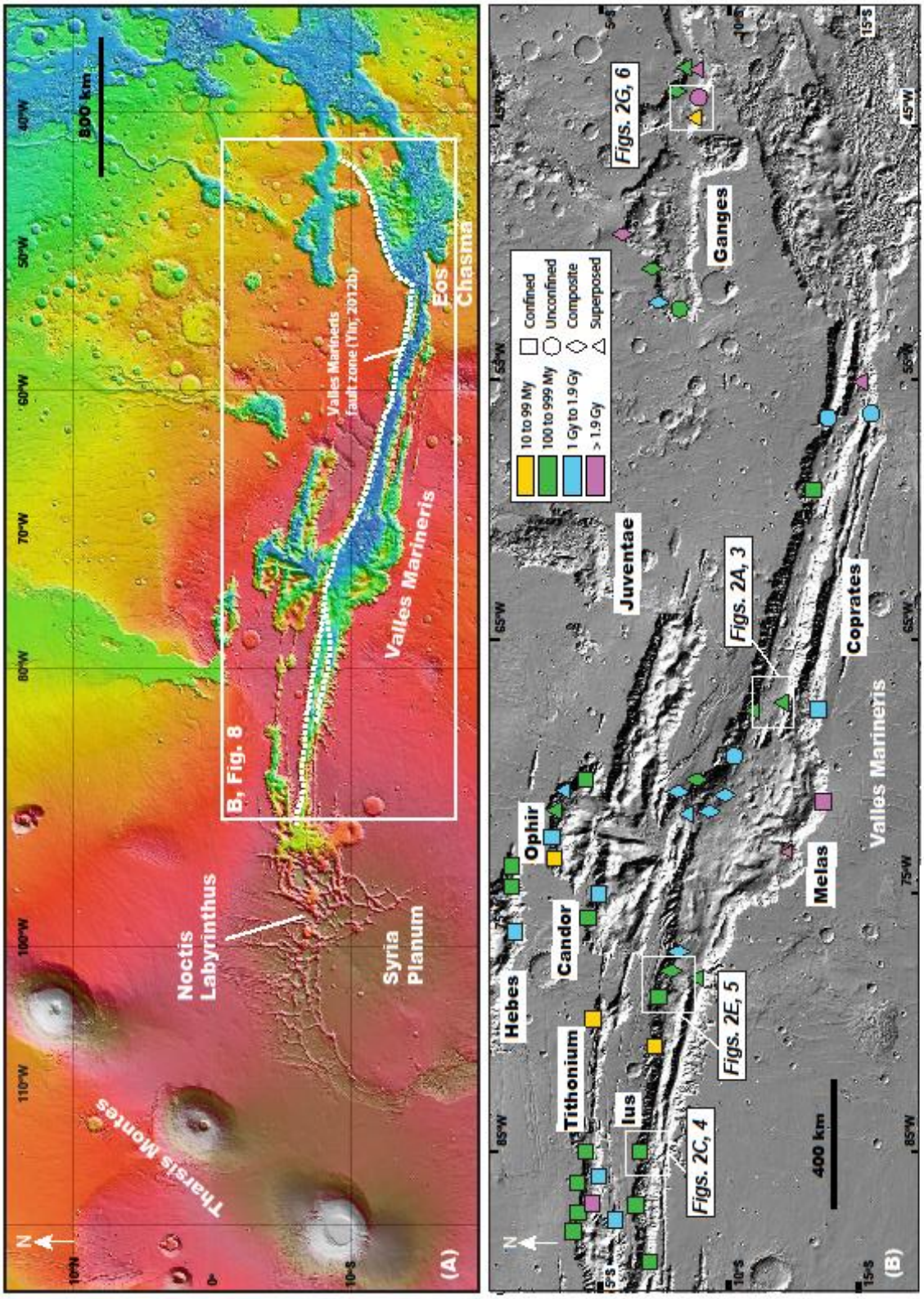

Watkins et al. Fig. 1

Figure 1. **Geologic setting and distribution of long-runout landslides in Valles Marineris.** (A) Regional topographic map of the Tharsis Rise and locations of B and Fig. 8. Valles Marineris lies at the equator and is bounded by a linear fault system at the base of the trough walls (Yin, 2012b). (B) Landslide locations, ages, and classifications in VM (after Quantin et al., 2004b). Landslides are classified as confined (squares) if transport of the outer zone was impeded by a topographic barrier, composite (diamonds) if multiple landslide outer zone lobes source from the same breakaway scarp, superposed (triangles) if the outer zone was deposited on the surface of a younger landslide debris apron, and unconfined (circles) if otherwise. Colors correspond to landslide surface ages with warmer colors representing younger deposits. The locations of Figs. 2-6 are also noted.

et al., 2006), leading to diverse models for their formation and transport mechanisms. The well-preserved nature of VM landslides lends insight into long-runout landslide emplacement on other planetary surfaces (e.g., Singer et al., 2012), and may have implications for past Mars climate.

What controls VM landslide morphology and mobility remains controversial. Major models for their emplacement mechanisms include: (1) basal lubrication by the presence of low-friction materials such as ice, wet materials, or clay minerals (Shaller, 1991; De Blasio, 2011; Watkins et al., 2015; Erismann, 1979), and (2) fluidization of fragmented landslide materials with (Harrison and Grimm, 2003; Lucchitta, 1979; 1987; Quantin et al., 2004a; Legros, 2002; Roche et al., 2011) or without (Melosh, 1979; 1987; McEwen, 1989; Soukhovitskaya and Manga, 2006; Hsü, 1975; Lajeunesse et al., 2006; Johnson & Campbell, 2017) the presence of water and volatiles. The possible involvement of ice and water in landsliding would require that climate conditions played a key role in shaping VM landslide morphology by enabling the episodic availability of lubricating materials for long-distance landslide transport, such as near-surface ice (e.g., Lucchitta, 1987; Peulvast and Masson, 1993; Gourronc et al., 2014), glaciers (Mège and Bourgeois, 2010), or the percolation of groundwater (e.g., Harrison and Chapman, 2008; Nedell et al., 1987; Lucchitta et al., 1994) in Valles Marineris. Important constraints on the VM landslide emplacement mechanisms are: (1) VM landslide location is not spatially correlated with age (**Fig. 1B**) (Quantin et al., 2004b) and (2) landslides of all ages share similar surface morphology (e.g., Lajeunesse et al., 2006; Lucas and Mangeney, 2007). This suggests that all VM landslides have a common and time-independent emplacement mechanism, and therefore, that they were emplaced under similar climatic conditions or that climate had no influence on emplacement.

In contrast, there is clear evidence that landslide breakaway-zone characteristics may influence VM landslide occurrence as indicated by their spatial distribution. That is, there is an evident paucity of landslides in eastern VM (**Fig. 1B**). Although this might be a result of fluvial erosion during the inferred catastrophic flooding that created the circum-Chryse outflow channels in the Late Hesperian (e.g., Warner et al., 2013; Harrison and Chapman, 2008), this explanation alone is unsatisfactory as the less-dissected Coprates Chasma is also devoid of remnant landslide breakaway scarps. Thus, lateral variation in trough-wall mechanical strength (Bigot-Cormier and Montgomery, 2007), local topography/relief and landslide breakaway-zone geometry (Lucas and Mangeney, 2007; Lucas et al., 2011), and/or seismic activity, as is implied by the close spatial correlation between VM landslides and steep, fresh escarpments interpreted as active, trough-bounding fault scarps (**Fig. 1**) (Blasius et al., 1977; Mège and Masson, 1996; Peulvast et al., 2001; Peulvast and Masson, 1993; Quantin et al., 2004a,b; Lucchitta, 1979; Yin, 2012b), must have also controlled VM landslide distribution. Conversely, a lack of spatial correlation between landslides and major craters has ruled out cratering as a cause of landslide initiation (Akers et al., 2012).

Previous efforts to identify the control(s) on VM long-runout landslide morphology have been limited by the lack of constraints on the quantitative morphometry at high resolution on a regional scale and, with one exception focusing largely on a single landslide (Watkins et al., 2015), on mineralogical composition of VM landslides, their source rock, and their basal zone materials. As a result, key questions such as the role of rock/sediment composition in controlling VM landslide map-view shape, surface morphology, and transport distance remain unanswered. In this study, we address this issue by conducting systematic geologic mapping with high-resolution Mars Reconnaissance Orbiter (McEwen et al., 2007; Malin et al., 2007), Mars Global

Surveyor (Christensen et al., 2004), and Mars Express (Neukum and Jaumann, 2004) imagery focused on the contact relationships between select VM landslides and their surrounding regions. We then parameterize and quantify key morphologic properties of the investigated landslides, and integrate compositional analysis of VM landslide vicinities using shortwave-infrared spectral data collected by the Compact Reconnaissance Imaging Spectrometer for Mars (CRISM) (Murchie et al., 2007). The integration of geological mapping and compositional analysis provides insight into the correlation of VM landslide morphology with the presence/absence of hydrated minerals, enabling constraint of VM landslide long-distance transport mechanisms.

2. Data and Methods

We integrate two approaches to investigate VM long-runout landslide emplacement mechanisms: (1) systematic mapping and quantification of landslide morphology, and (2) correlation of landslide morphology to landslide (including the basal shear zone) mineralogical compositions. The first task was performed through interpretation of Thermal Emission Imaging System (THEMIS), Context Camera (CTX), High Resolution Imaging Science Experiment (HiRISE), and High Resolution Stereo Camera (HRSC) images, while the second task was accomplished by analyzing coupled CRISM shortwave-infrared spectral data, when available.

2.1 Data and Methods of Geological Mapping

Each orbital imager utilized by this study provides various advantages for mapping the field relationships and quantifying the morphology of the landslides. HiRISE images are ~25 cm/pixel (McEwen et al., 2007), useful in analyzing detailed stratigraphic and structural relationships as well as defining subtle morphologic features within a landslide. CTX images are ~6 m/pixel,

well-suited for mapping the contextual geology of an individual landslide (Malin et al., 2007). THEMIS visible images at ~18 m/pixel are most useful for correlating regionally extensive units between landslides (Christensen et al., 2004). HRSC images are ~12 m/pixel (Neukum and Jaumann, 2004), often acquired in stereo pairs, and along with MOLA gridded topographic data (Zuber et al., 1992) enable 3-D quantification of structures based on their geometric interactions with topography. Higher resolution CTX image mosaics were constructed and registered to HRSC digital terrain models (DTMs) that allow orientation determination (strike and dip) of planar geologic features using the ORION software available from Pangaea Scientific (e.g., Fueten et al., 2005; 2008). Our mapping procedure follows that of Schultz et al. (2010) and Yin (2012b), which allows the translation of morphologic features to corresponding geologic structures.

2.2 Methods of CRISM Data Analysis

The CRISM instrument is a visible-infrared imaging spectrometer with targeted observations taken in 544 channels in the visible to shortwave-infrared (VSWIR) (Murchie et al., 2007). It acquires observations in both 18-40 m/pixel targeted and 100–200 m/pixel mapping modes. The "S" detector covers the 0.4-1.0 μm visible/near-infrared (VNIR) spectral range and the "L" detector covers the 1.0-4.0 μm SWIR spectral range. This study analyzes "L" detector Targeted Reduced Data Record (TRDR) observations over the 1.0-2.6 μm spectral range, which is best-calibrated, least sensitive to dust cover, and its effectiveness has been demonstrated in previous studies for the detection of hydrated silicates, hydrated sulfates, and mafic minerals (e.g., Murchie et al., 2009a,b). CRISM's high spatial resolution makes it ideal for the collection of robust spectra of discrete compositional units within a deposit (e.g., Roach et al., 2010).

Spectral analysis of morphologic end-members at all sites where landslides and their surrounding regions are well-exposed and for which CRISM full-resolution target (FRT) or half-resolution long observation (HRL) images exist was completed. A total of 51 CRISM images were examined, exhausting the available long-wavelength channel CRISM coverage of long-runout landslides and their immediate vicinities in VM as of September 2015 (**Table 1**). Using the CRISM Analysis Toolkit (CAT) produced by the CRISM Science Team (Murchie et al., 2009b), standard CRISM photometric and atmospheric corrections to the raw data were applied to each image by dividing each pixel by the cosine of the incidence angle and by a scaled atmospheric transmission spectrum derived from observations of Olympus Mons (e.g., Mustard et al., 2008). Spectra of interest were generated by averaging signals in an area of 7 x 7 pixels. The signals were then normalized by dividing the spectra of interest by the spectrum of a spectrally neutral or unremarkable region (usually corresponding to Mars dust) in the same detector column. This procedure enhances spectral differences between areas of different geologic units and removes residual atmospheric and instrument artifacts (e.g., Roach et al., 2010). These ratioed spectra were then compared to RELAB and USGS library laboratory reflectance spectra within the wavelengths of CRISM data for potential matches in diagnostic absorption band locations and spectral shapes.

Minerals are detected by recognition of electronic transition absorptions from iron and vibrational overtones and combination tones from, e.g., OH and H_2O in minerals (Burns, 1993; Clark et al., 1990). Specific hydrated minerals possess unique and characteristic spectral signatures. Water in mineral structures has an absorption between 1.91 and 1.95 μm due to H_2O vibration that is observed and mapped in CRISM data. In Valles Marineris, also commonly observed is a weaker absorption between 1.40 μm and 1.45 μm, due to H_2O or metal-OH

CRISM image ID	Location in VM	Hydrated minerals detected?
HRL00008554	Tithonium Chasma	N
FRT00008FF0	Ius Chasma	Y
FRT000088FC	Ius Chasma	Y
FRT00013EDE	Ius Chasma	Y
FRT00009C50	Ius Chasma	Y
HRL0000D0E3	Ius Chasma	N
FRT0000D740	Ius Chasma	Y
FRT0000A396	Ius Chasma	Y
FRT0000C119	Ius Chasma	Y
FRT00018FD5	Ius Chasma	Y
FRT000027E2	Ius Chasma	Y
FRT0000905B	Ius Chasma	Y
HRS0001E247	Ius Chasma	Y
FRT0000B939	Ius Chasma	Y
HRL00007AA5	Ius Chasma	N
FRT0000A834	Ius Chasma	N
FRT0001883A/FRT0000D243	Ius Chasma	N
FRT0000BDF1	Ius Chasma	N
FRT00016B12	Melas Chasma	Y
FRT00018067	Melas Chasma	Y
FRT0000AA51	Melas Chasma	Y
HRL0000C2BA	Melas Chasma	N
HRL000121B5	Melas Chasma	N
FRT00010F86	Melas Chasma	Y
FRT00010FF8	Melas Chasma	N
FRT0000B510	Coprates Chasma	N
HRL0000B2AB	Coprates Chasma	N
FRT000195E8	Coprates Chasma	N
HRS00019765	Coprates Chasma	N
FRT0001892B	Coprates Chasma	N
HRL00019505	Coprates Chasma	N
FRT00009D64	Coprates Chasma	N
FRT00006419	Coprates Chasma	N
FRT000093E3	Coprates Chasma	Y
FRT00016CDA	Coprates Chasma	N
HRL0000A8F6	Coprates Chasma	Y
FRT0000A55E	Ganges Chasma	N
HRL0000B48A	Ganges Chasma	Y
FRT000136CF	Ganges Chasma	Y
HRL0000BF5A	Ganges Chasma	N
FRT0001693A	Ganges Chasma	Y
HRS0000B146	Ganges Chasma	N
HRL0000A432	Ophir Chasma	Y
HRL0000508A	Ophir Chasma	Y
HRL0000C30D/HRL0000C59C	Ophir Chasma	N
FRT0000BB63	Ophir Chasma	N
FRT0001672B	Ophir Chasma	N
FRT000175E0/FRT00016943	Candor Chasma	Y
FRT0000BB2A	Candor Chasma	N
HRL00019711	Candor Chasma	N
FRT00016DC9	Hebes Chasma	N

Watkins et al. Table 1

vibrations. A sharp doublet with minima near 2.21 μm and 2.278 μm (due to metal-OH vibrations) and an inflection around 2.4 μm are spectral signatures consistent with the presence of a class of hydrated silicate material previously identified in Ius, Coprates, and Melas Chasmata and Noctis Labyrinthus (Roach et al., 2010; Metz et al., 2010; Weitz et al., 2011; 2014). This "doublet material" does not show a good spectral match to any single library spectra, and is thought to contain some mixture of hydrated silica, Fe-smectite, possibly partially altered, and jarosite (Roach et al., 2010; Thollot et al., 2012). A broad absorption between 2.20 μm and 2.26 μm indicates the presence of structural H_2O in sulfates, a hydrated signature evident in the library reflectance spectra of hydrated minerals such as monohydrated sulfates (kieserite), also found in Valles Marineris (Roach et al., 2010). In other VM materials, an absorption at 2.3 μm is a spectral signature of Fe/Mg-OH, such as in Fe/Mg phyllosilicates previously found at the foothills of Ius Chasma (Roach et al., 2010), in dark boulders and associated dusty talus in the mid to lower walls of western VM (Flahaut et al., 2012), in troughs and a closed depression in Noctis Labyrinthus (Thollot et al., 2012; Weitz et al., 2011), in lower parts of Coprates Chasma walls and landslides (Murchie et al., 2009a), and in globally widespread exposures of Noachian bedrock (e.g., Ehlmann et al., 2011).

Spectral summary parameters were calculated from diagnostic absorptions to distinguish between these minerals and facilitate preliminary identification and mapping of distinct geologic regions within a CRISM image (e.g., Pelkey et al., 2007). Summary parameters used in this study include the 1.9 μm band depth (BD1900), the 2.21–2.27 μm band depth (BD2200), and the 2.3 μm band depth (D2300) (e.g., Roach et al., 2010) and were configured to highlight spectral end-members distinguished mostly by water content. Map-projected composition data were integrated with geologic maps created by interpreting CTX, HiRISE, THEMIS, and HRSC

orbital imagery. Geologically-defined end-member units based on the relationships in both the satellite images and summary parameter images were mapped. Morphological indicators of CRISM-defined spectral units were used for geologic mapping outside the extent of CRISM observations.

2.3 Methods of Morphological Quantification and Classification

The most dominant mass wasting processes in VM can be broadly divided into two types: (1) debris flows that consist of a steep, debris-loaded, U-shaped, eroded channel and a small depositional fan with coarse levees and high slope angles (Lucchitta, 1979; Brunetti et al., 2014; Hungr et al., 2014) and (2) long-runout landslides, which consist of a large (>1 km) coherent rock mass, are the focus of this work, and are described in detail below. The debris flows are volumetrically much smaller (average deposit surface area of 50 km^2) than long-runout landslides (average deposit surface area of 1090 km^2). We adopt the two-zone classification of long-runout landslides of Watkins et al. (2015), consisting of an arcuate breakaway scarp and two distinct zones, inner and outer, of the landslide mass (**Fig. 2**).

We classify VM long-runout landslides into four types: (1) unconfined, (2) confined, (3) composite, and (4) superposed subclasses (**Fig. 2**). An *unconfined landslide* is one that has an unimpeded front and whose geometry is fully displayed on the VM trough floor (circles in **Fig. 1B**). An example of this type of landslide is located in Coprates Chasma and shown in **Figs. 2A, 2B, and 3**. A *confined landslide* is one whose front is impinged and thus confined by a topographic high (squares in **Fig. 1B;** see example in **Figs. 2C, 2D, and 4**). A *composite landslide* is one in which more than one overlapping debris apron is sourced from the same breakaway scarp (diamonds in **Fig. 1B**; see example in **Figs. 2E, 2F, and 5**). A composite

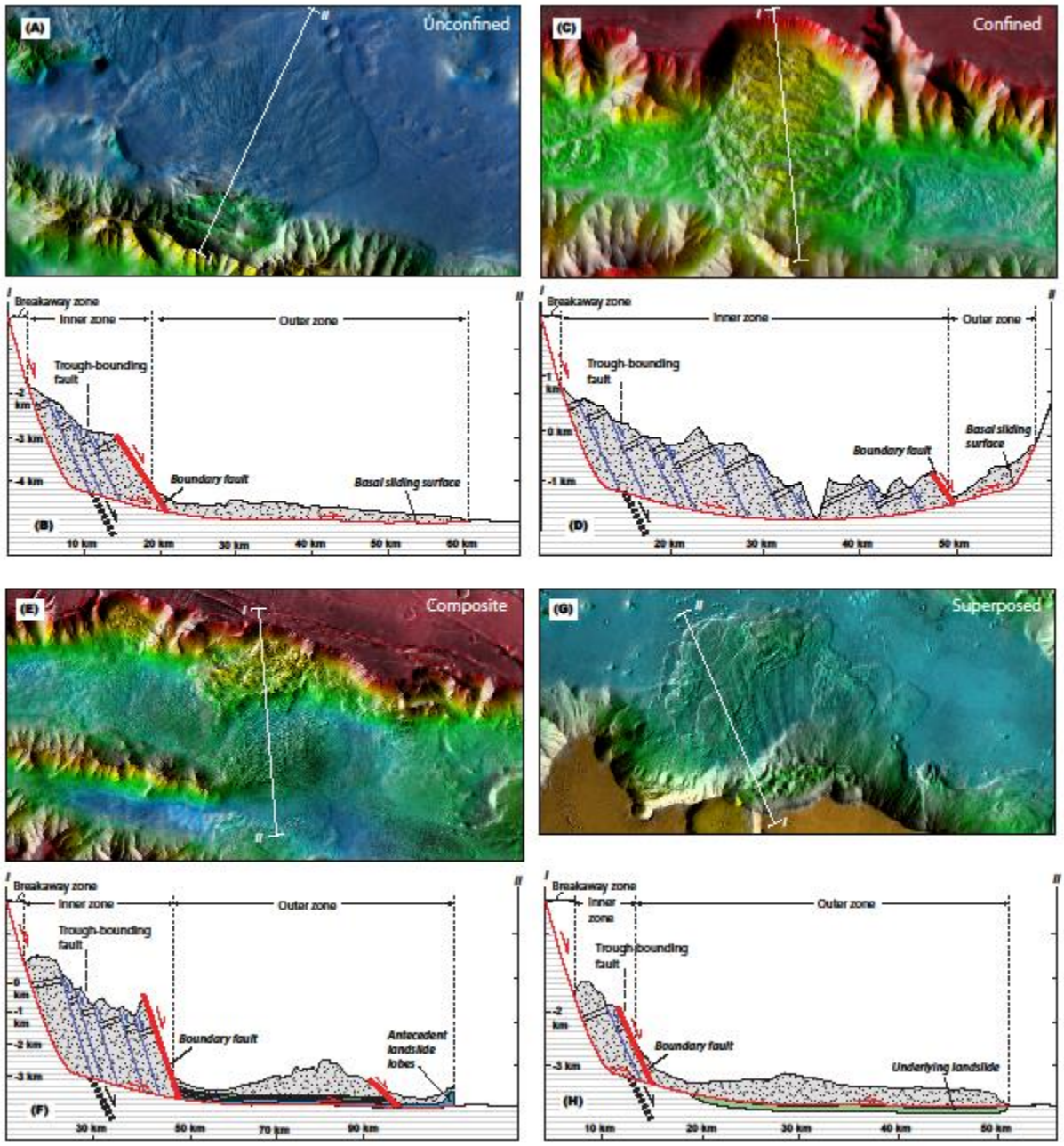

Watkins et al. Fig. 2

Figure 2. VM long-runout landslide classifications. MOLA topographic color is overlain on THEMIS Day IR mosaics of (A) unconfined, (C) confined, (E) composite, and (G) superposed landslide examples (see Fig. 1 for locations). Cross sections are interpreted using MOLA topographic data through (B) mosaic in A, (D) mosaic in C, (F) mosaic in E, and (H) mosaic in G. Previously emplaced landslide lobe colors correspond to detailed sequential evolutions in Figs. 5C and 6C.

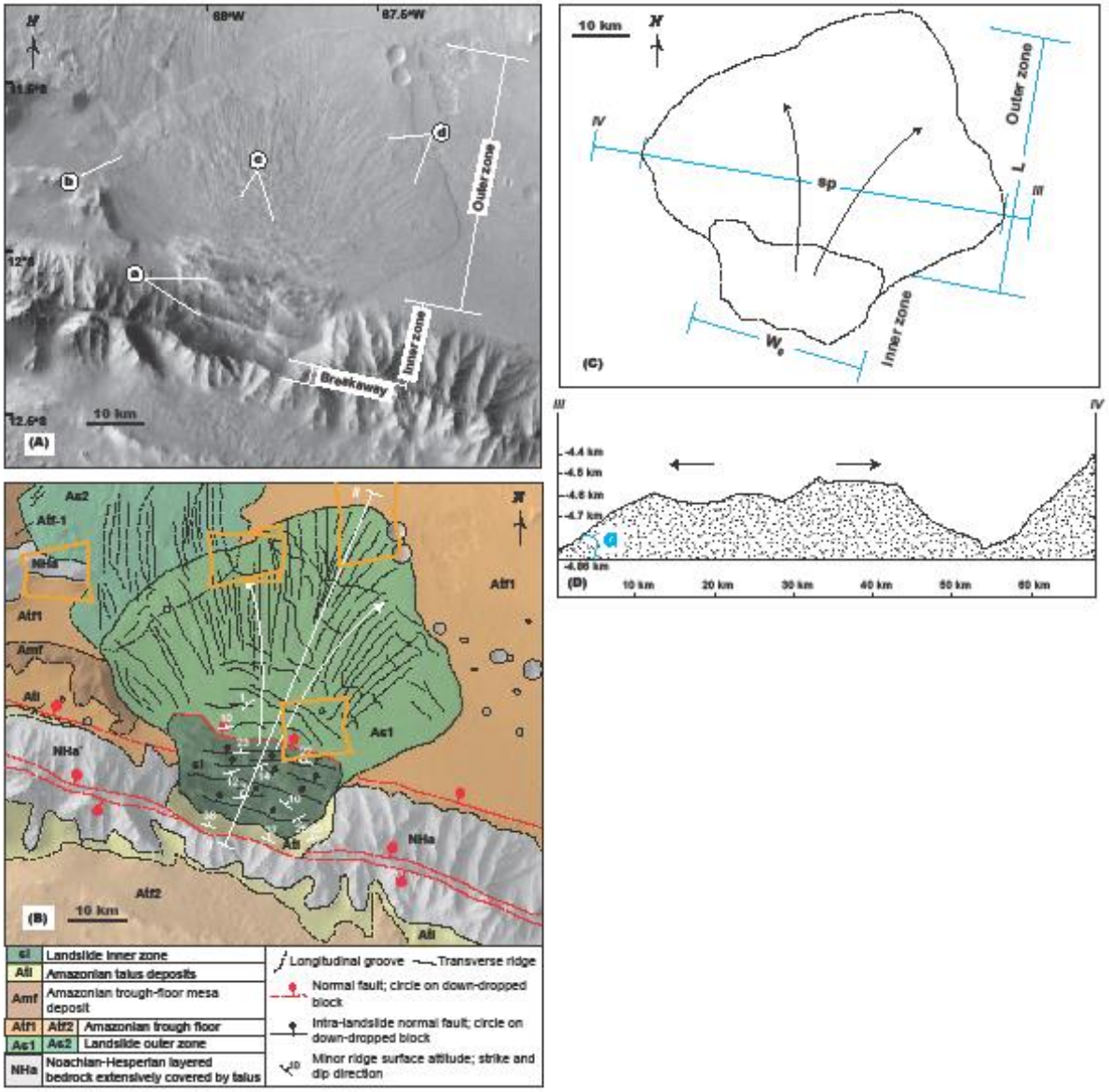

Watkins et al. Fig. 3

Figure 3. **VM long-runout landslide morphological structure.** (A) THEMIS mosaic of unconfined VM long-runout landslide example in Coprates Chasma, indicating morphological features *a*, tilted blocks, *b*, thinness of the deposit at the toe, evident where the younger landslide deposit is visibly superposed on the apron of an older slide, *c*, radial fractures, and *d*, longitudinal ridges and grooves, as well as the inner, outer, and breakaway zones. (B) Detailed geologic map of units and features in A. Red dashed line follows trace of trough-bounding and intra-landslide normal faults. Circles are on the down-dropped block. Arrows indicate transport direction. Calculated surface attitudes of the minor transverse ridges formed by the tilted blocks are shown. Also shown are the locations of CRISM images within the map region analyzed in this study.

Orange boxes indicate CRISM image examined (no hydrated mineral detections). (C) Landslide inner and outer zone outline with definitions of measured VM long-runout landslide geometric parameters in plan view: *sp*, spreading width, *L*, runout length, W_0, breakaway-scarp width. Location of the profile in E is also shown. (D) Landslide cross section with topographic profile derived from MOLA data, defining measured VM long-runout landslide geometric parameter α, surface slope angle, in cross-sectional view. Arrows indicate lateral spreading perpendicular to landslide transport.

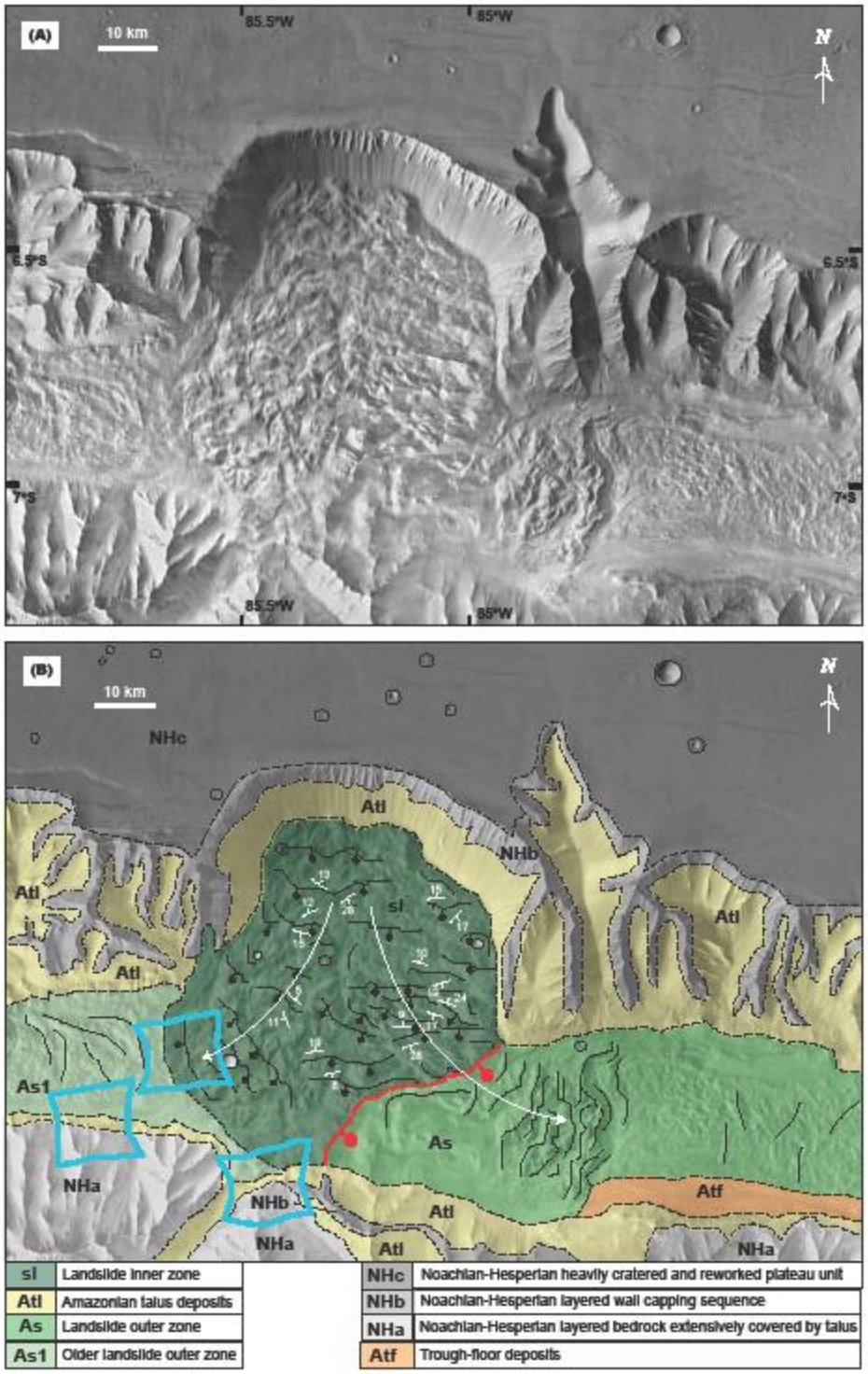

Watkins et al. Fig. 4

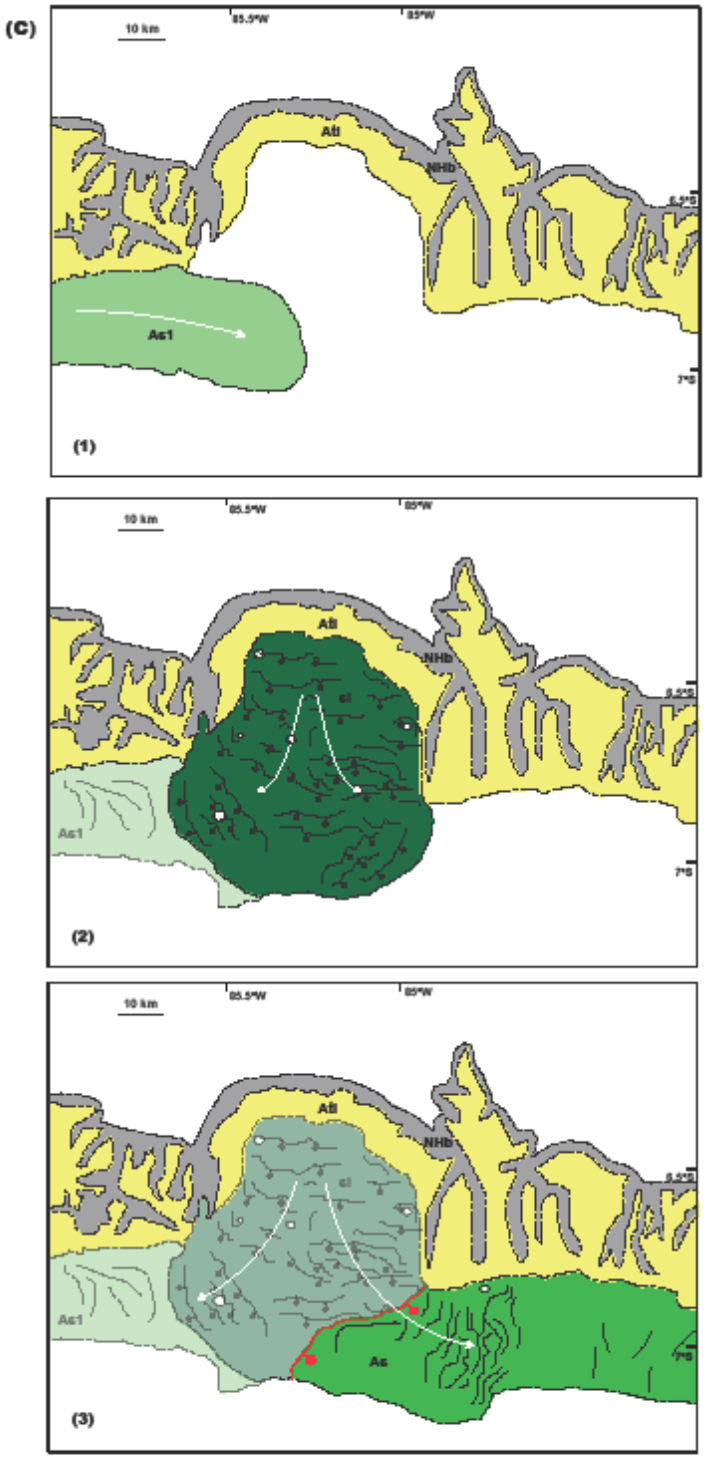

Watkins et al. Fig. 4, cont.

Figure 4. **Confined VM long-runout landslide classification example**. (A) Confined type in Ius Chasma (THEMIS mosaic). (B) Geologic map of landslide in A. Red dashed lines indicate main intra-landslide boundary fault scarp; black dashed lines indicate minor scarps and ridges;

arrows indicate landslide transport direction. Circles on down-dropped block. Long-dashed lines indicate longitudinal grooves. Blue boxes indicate CRISM images with hydrated mineral detection. (C) Example sequential evolution of the confined landslide complex in A and B, with inferred original lobe geometries.

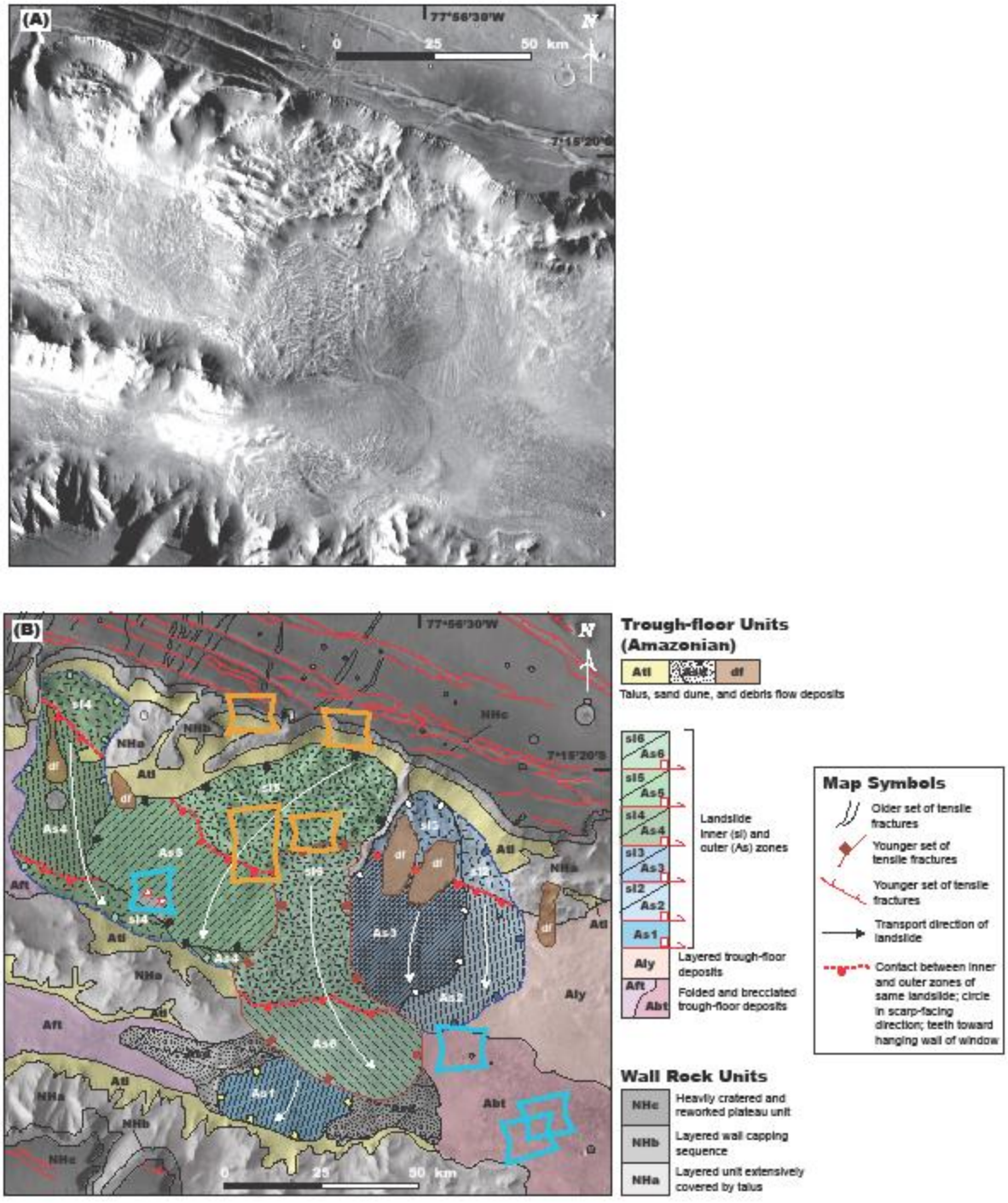

Watkins et al. Fig. 5

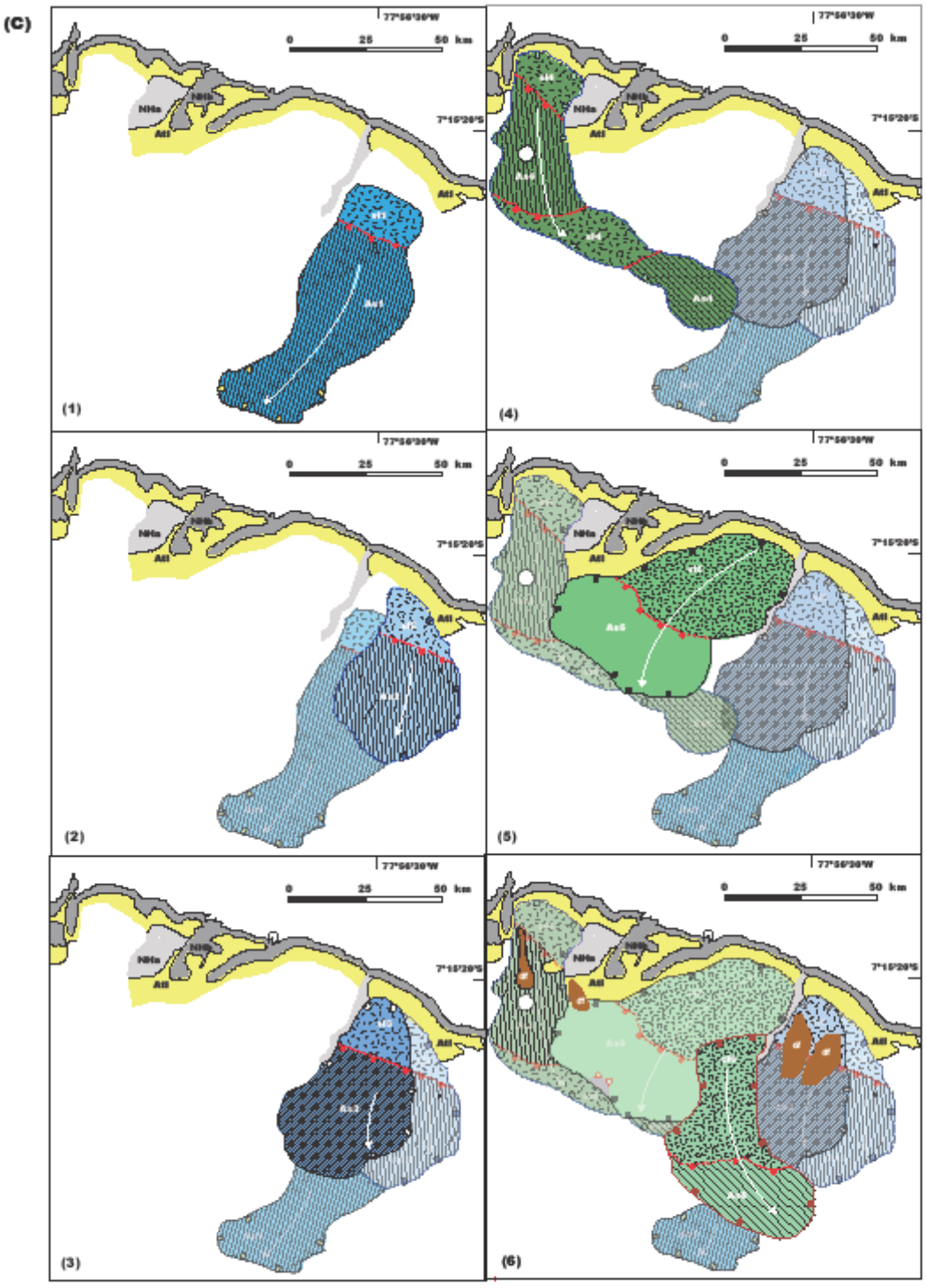

Figure 5. **Composite VM long-runout landslide classification example**. (A) Composite type in eastern Ius Chasma (THEMIS mosaic). (B) Geologic map of landslide complex in A. (C)

Example sequential evolution of the composite landslide complex in A and B, with inferred original lobe geometries.

landslide may be partially confined or unconfined. Lastly, we define a *superposed landslide* as one that overrode an older landslide with a different source area (triangles in **Fig. 1B;** see example in **Figs. 2G, 2H, and 6**). Superposed landslides may also be confined or unconfined.

We quantify landslide morphology using the following geometric parameters (**Fig. 3C**): (1) the maximum outer zone runout length (L) from the intra-landslide boundary fault scarp to the toe, (2) the maximum exposed outer-zone spreading width (sp), which in combination with L represents the overall landslide mobility, (3) the width of the breakaway scarp along which the landslide material was displaced (W_0), which is used as a proxy for the volume of the mobilized landslide mass, and (4) the minimum surface slope angle (α). The surface slope angle α of the lateral spreading zone provides a proxy for estimating the basal friction of the landslide outer zone. This is because the highly fragmented outer zone can be treated as plastic material with internal and basal yield strengths, much like a glacier. In order for glaciers to flow, the gravitationally induced stress, represented by the surface slope, must be balanced by the shear resistance at the base (e.g., Clarke, 2005). This leads to the relationship $\boldsymbol{\mu = \sin(\alpha)}$, where $\boldsymbol{\alpha}$ is the surface slope measured perpendicular to the sliding direction of the outer zone. We measured geometric properties of landslides on mosaicked CTX images overlain on MOLA topographic data in JMARS (Java Mission-planning and Analysis for Remote Sensing).

3. Results

3.1 Geological Mapping of Landslides

The characteristic two-zone surface morphology identified by Watkins et al. (2015) is ubiquitous in VM landslides of diverse ages and is characterized by the presence of tilted slump blocks in the inner zone (e.g., feature *a* in **Figs. 3A and 3B**) and a lobe-shaped outer zone

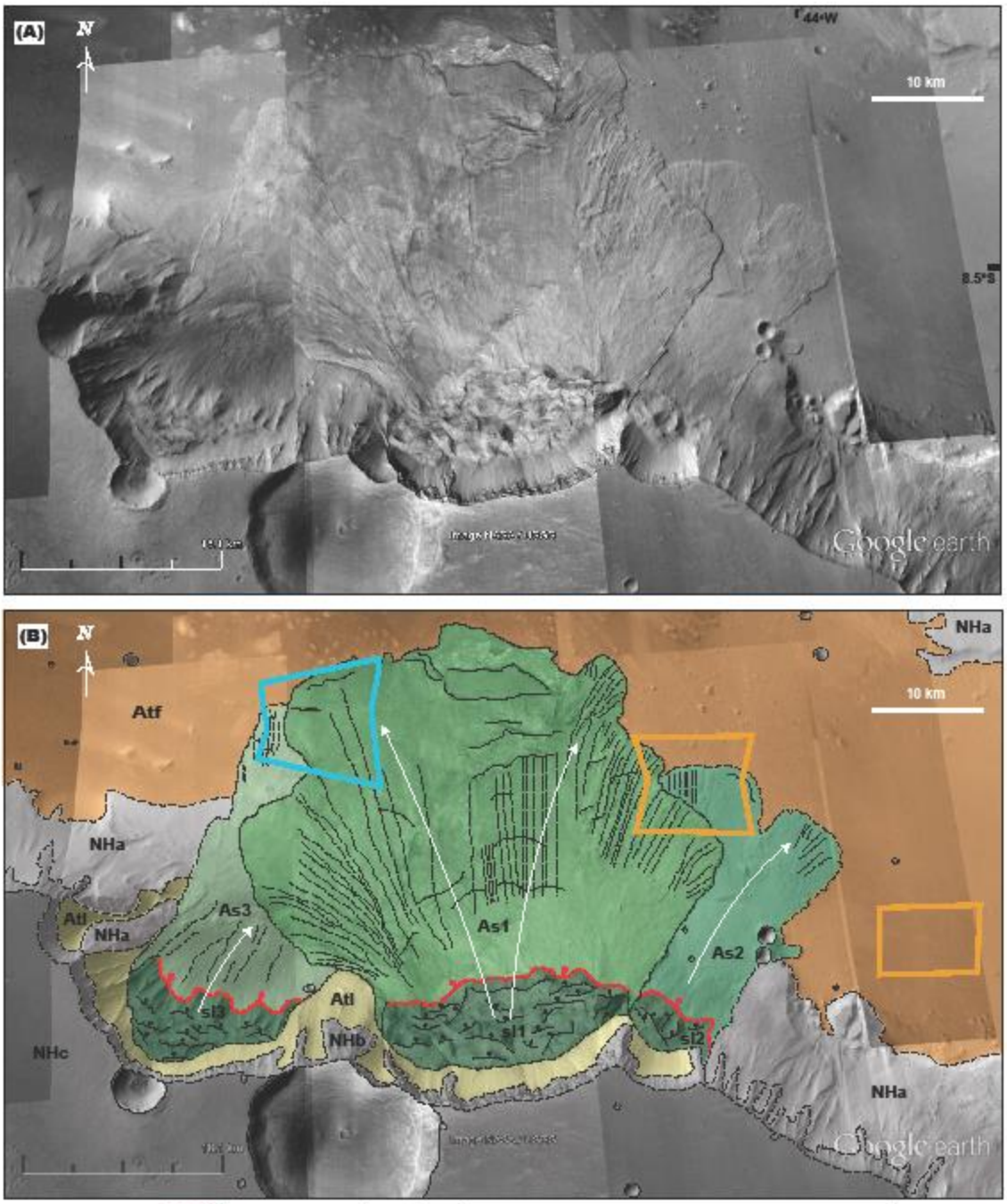

Watkins et al. Fig. 6

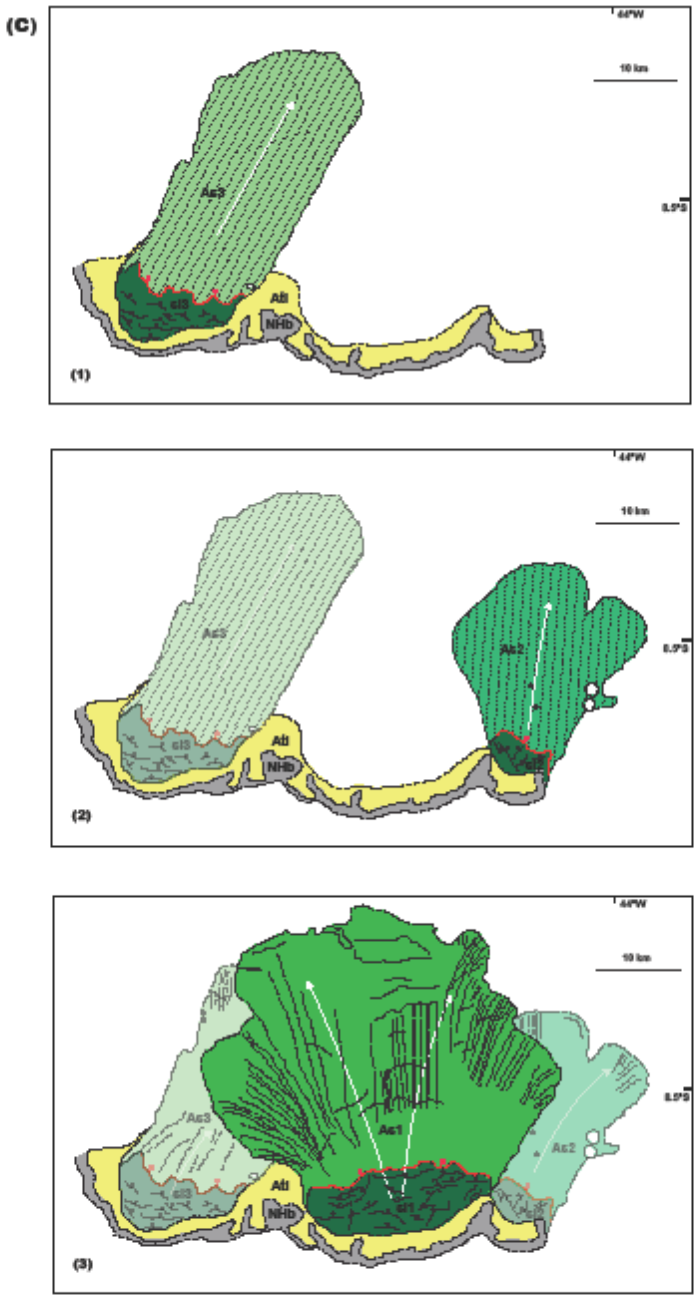

Watkins et al. Fig. 6, cont.

Figure 6. Superposed VM long-runout landslide classification example. (A) Superposed type in Ganges Chasma (CTX mosaic). (B) Geologic map of landslide in A. Despite variation in classification, VM long-runout landslides share characteristic morphologic features. (C) Example sequential evolution of the superposed landslide complex in A and B, with inferred original lobe geometries.

(feature *b* in **Fig. 3A**). The tilted blocks in the inner zones are typically < 10 km from their source regions and their crests strike parallel to the breakaway scarp and intra-inner-zone faults. The tilting of the slump blocks was most likely induced by motion along a concave upward basal slip surface that links the steep breakaway scarp and the sub-horizontal trough floor (e.g., Highland and Bobrowsky, 2008) (**Fig. 2B**). In contrast, the outer zones display chaotically distributed, fragmented landslide materials with individual blocks 100s to 10s of meters in size. The outer zones are much longer in the landslide transport direction than the inner zones, and the overall length vs. width aspect ratio of VM landslides is much larger than similar landslides on Earth, as noted by Lucchitta (1978), (1979), and (1987). In addition, the outer zone surfaces exhibit convex-forward transverse (feature *c* in **Fig. 3A**) and longitudinal ridges (feature *d* in **Fig. 3A**), separated by V-shaped grooves, that diverge in a vast debris apron radiating from the source region and locally curving to form separate lobes. At the toe of an outer zone lobe, either transverse ridge formation or soft-sediment deformation dominates, depending on whether landslide-related compression causes material to pile up. That $sp > W_0$ implies significant lateral spreading of the outer zone during landslide runout, supported by an increase in total landslide volume from the initial to the final state (Lucas et al., 2011).

Although VM landslides are all characterized by the two-zone morphologic division, they display unconfined, confined, composite, and superposed subclasses (as discussed in section 2.3 and shown in **Fig. 2**), are controlled by distinct kinematics, and demonstrate considerable spatiotemporal variability in geometric parameters. A landslide in Coprates Chasma (**Fig. 3**) exemplifies the unconfined landslide type, in which the transport of the outer zone was unimpeded by any topographic barrier. In this case, the only governing parameters in stopping landslide motion, thus dictating runout length, *L*, were internal and sliding surface resisting

forces. Crater counting on the surface of this landslide yields an estimated surface age of ~400 Ma (Quantin et al., 2004b). It occurs on a central ridge within the trough, which consists of Noachian-Hesperian layered bedrock (*NHa*) dissected by prevalent spur-and-gully erosion and extensively covered by talus (*Atl*) (**Fig. 3B**). The breakaway scarp, whose surface trace is more linear than semi-circular, occurs along a fault that runs the length of the ridge crest. Faults were found to be associated with the breakaway scarps of 18 of 33 unconfined landslide lobes. The steep breakaway surface of the Coprates landslide incises the entire trough wall down to its base, causing the evacuation of landslide materials from the entire trough-wall section upon initiation (**Fig. 2B**). This is the case for 44 of the 50 VM landslides surveyed.

As is characteristic for all VM landslides, the talus-covered breakaway scarp lacks the spurs and gullies that modify the adjacent walls, implying emplacement after major dissection of the trough walls (Lucchitta et al., 1992). Spreading outward from the typical inner zone (*sl*) and ~1.5-km intra-landslide fault scarp is the outer zone (*As1*), which overrode a smooth, minimally-scoured trough-floor unit (*Atf1*) and an older landslide outer zone (*As2*), as is evident by the overprinting of an older lobe and its longitudinal grooves (feature *b* in **Fig. 3A**). The locations of analyzed CRISM images covering units related to this landslide within the map region are shown in **Fig. 3B**.

A landslide in western Ius Chasma (**Fig. 4**) and its juxtaposition with a topographic barrier in the valley illustrate the characteristics of the confined landslide subclass. In this case, the inner zone reached a barrier, causing the transport of the outer zone material to be deflected "downstream" along the canyon (see **Fig. 2D**). Because of this, the runout length *L* was not solely dependent on the work done by basal friction. This particular landslide is dated as ~ 800 Ma by crater-counting estimate (Quantin et al., 2004b) and was initiated along the trough wall of

western Ius Chasma consisting of a Noachian-Hesperian layered sequence (*NHb*) and a Noachian-Hesperian heavily cratered and reworked plateau unit (*NHc*). The trough walls around the landslide have been extensively modified by fluvial erosion, forming spur-and-gully morphology, sapping channels, and widespread talus deposits (*Atl*). The breakaway scarp of this landslide does not occur along an observable fault, and the scarp surface trace is amphitheater-shaped (**Fig. 4B**). An incipient breakaway is also visible on the plateau west of the landslide scarp. As is the case for the unconfined example, the rotated blocks of the confined landslide inner zone (*sl*) strike perpendicular to the direction of transport. However, upon encountering the central ridge, landslide transport was diverted along the trough floor with the inner zone overriding an older landslide outer zone (*As1*) to the west and the hummocky outer zone (*As*) riding over trough-floor deposits (*Atf*) to the east (**Fig. 4C**). Subsequently, both units *As* and *Atf* were faulted (Yin, 2012b), eroded, and partially covered by dust and sand dunes. In CRISM images covering this landslide **(Fig. 4B)**, hydrated silicate and smectite are detected in the *As1* outer zone onto which the younger landslide inner zone (*sl*) was emplaced.

The evolution of a composite landslide is illuminated by the example in eastern Ius Chasma (**Fig. 5**). Composite landslide inner zones resemble that of other types, and are similarly separated from outer zones by a major fault scarp. Although the transport directions of the debris aprons that comprise the landslide system may differ, the observed morphologies could have formed from a single emplacement event that occurred between 100-200 Mya (Quantin et al., 2004b) and was comprised of multiple pulses or surges and points of scarp failure, leading to the overlapping of lobe deposits. Long periods of time between lobe emplacements are not required. Each of the debris aprons originally sourced from the walls of eastern Ius Chasma, which consist of Noachian-Hesperian wall rock units *NHa*, *NHb*, and *NHc*, and, as in western Ius, have been

extensively eroded. A distinct spatial relationship between putative left-lateral, transtensional (Yin, 2012b) trough-bounding faults and the linear landslide breakaway-scarp surface trace is observed (**Fig. 5B**). The prevalence of these faults may also explain the ubiquity of landslides in this region. Most of the breakaway surfaces associated with this landslide complex cut all the way down to the trough floor, but the breakaway scarp of landslide *As4* is instead separated from the base of the wall by a steep, secondary scarp. This indicates that this landslide was launched from a shallower depth in the upper section of the trough wall, as were 6 others out of 50 VM landslides. The general morphology of the landslide systems initiated from the upper versus whole sections of the trough walls is similar.

The interpreted sequential emplacement of the landslide complex in eastern Ius Chasma, based on transport direction inferred from deposit lobe shape, lobe cross-cutting relationships, and degree of lobe weathering, is as follows (**Fig. 5C**): (1) *As1* was deposited, though its source region is not clear, (2) *sl2* was initiated and emplaced, followed by *As2* onto layered and brecciated trough-floor deposits (*Aly* and *Abt*, respectively), (3) likely in quick succession, wall material adjacent to the original *sl2* breakaway zone failed, forming *sl3* along the same scarp as *sl2*, and *As3* which overrode the *As2* lobe, (4) *sl4* was initiated and launched from the upper wall, rafting on top of *As4* which was emplaced over folded trough-floor deposits (*Aft*), (5) additional wall rock abutting the original *sl2* breakaway zone failed, forming *sl5* along the same scarp as *sl2* and *sl3*, and *As5* which overrode both zones of lobe 4, (6) an erosional window was formed at the toe of *As5*, uniquely exposing the basal sliding layer, (7) during emplacement of lobe 5, a portion of *sl5* failed, forming *sl6* which rode over older *As4* and *As3* lobes, and (8) *As6* was then emplaced over *As2*, *As1*, and brecciated trough-floor deposits (*Abt*). Sand dune (*Asd*) and debris flow (*df*) deposits later covered some landslide surfaces. Building on the analysis of CRISM

images of this landslide by Watkins et al. (2015), which identified hydrated silicate and smectite in the basal sliding zone of *As5*, we also detect these hydrated minerals in the *Abt* trough-floor unit, which *As2* overrode during emplacement (**Fig. 5B**; see section 3.3 for detailed compositional analysis).

A landslide complex in Ganges Chasma (**Fig. 6**) typifies the diagnostic cross-cutting relationship of superposed landslides, which requires sequential landslide emplacement from nearby sources. This landslide complex is estimated to be ~50 My old (Quantin et al., 2004b) and occurs along the walls of Ganges Chasma, which consist of Noachian-Hesperian units *NHa*, *NHb*, and *NHc*, but are not as extensively eroded as those in Ius Chasma as indicated by more subdued spur-and-gully morphology and few sapping channels. Although the breakaway scarps of this landslide complex are not spatially correlated with an observable trough-bounding fault, they do intersect large impact craters on the adjacent plateau (**Fig. 6B**). This proximity may suggest that in this particular case, impact-induced seismic shaking exerted key control on landslide initiation and the resulting arcuate breakaway scarp. Emplacement of the superposed landslide complex, as shown in **Figure 6C**, first requires the prior emplacement of both zones of a neighboring landslide (*As2* and *As3* in **Fig. 6C**) onto the trough floor (*Atf*). It is not known with certainty which of the two lobes was deposited first, but the higher degree of degradation of the wall rock associated with *As3* suggests that it is older. The inner zone (*sl1*) was then emplaced, followed by the formation of a fault scarp and emplacement of a characteristic outer zone (*As1*) which overrode underlying landslide lobes *As2* and *As3*. Hydrated minerals are detected in this study near the toe of *As1* where it overrode *As3* in a CRISM image within the map region of this landslide (**Fig. 6B**).

3.2 Quantifying Geometric Relationships of VM Landslides

The outer-zone geometry of 26 unconfined VM landslides is quantified using the morphologic parameters defined in the methods section above (also see **Table 2**). Where possible, surface slope angle (α) of the outer zone was measured at the intersection of the widest portion of the lobe, where it is spread the thinnest, and the underlying trough floor sliding surface, in order to estimate the minimum coefficient of basal friction of the lobe (**Fig. 3D**). To isolate the mechanical properties of each debris apron, all morphological parameters of composite and superposed landslides were measured for each individual lobe separately, including outer-zone spreading width (*sp*) and slope angle (α) on the trough floor. Because of confounding factors introduced by topography, confined landslides are not included in the compiled morphometric analyses.

By quantifying the landslide geometry, we find that VM landslide outer zones are exceptionally mobile compared to terrestrial examples that share morphological similarities (e.g., Blackhawk and Sherman landslides; Lucchitta, 1978) and compared to debris flows in VM (**Fig. 7A; Table 3**). Linear trend models enable quantification of the correlation between variables and provide insight into deviation of morphometric observations from known physical relationships. The lateral spreading width of the studied outer zones increases with runout length at a ratio of ~1:1.4 (**Fig. 7A**). In comparison, VM debris flows exhibit a ratio of 1:0.6, represented by a steeper curve in the log-log plot in **Figure 7A**. The lack of lateral spreading of smaller-volume debris flows in VM indicates that the lateral spreading width generally increases with increasing mass, supporting the conclusion reached by Lucas et al. (2011; 2014) that the mobility of large landslides is dependent on the

Chasma	*Latitude*	*Longitude*	*sp (m)*	*L (m)*	*Wo (m)*	*α (deg)*[1]	*Subclass*[2]	*Age (My)*[3]
Ganges	7° 55'14.22" S	41° 20' 59.47" W	13575	16629	5702		S	200
Ganges	8° 8'46.09" S	41° 20' 47.79" W	16426	20819	7193		S	3000
Ganges	7° 44'24.35" S	44° 12' 18.40" W	11369	25351	6570	4.704	C	700
Ganges	8° 36'21.99" S	44° 12' 14.05" W	18626	25403	7656	1.984	U	N/A
Ganges	8° 29'6.25" S	44° 34' 48.55" W	43009	35821	26132	6.156	S	50
Ganges	6° 21'59.12" S	49° 23' 48.16" W	34452	23568	23606		C	> 2000
Ganges	7° 29'26.95" S	50° 34' 13.79" W	26587	29154	14369	7.161	C	100
Ganges	7° 38'10.14" S	51° 49' 23.03" W	17341	39712	5072		C	> 1000
Ganges	8° 27'41.55" S	52° 15' 22.86" W	21851	25429	20089		U	> 200
Coprates	13° 11'42.18" S	59° 14' 38.78" W	24808	53614	10939	1.799	CF	150
Coprates	14° 42'40.86" S	56° 49' 45.15" W	39190	56381	12904	4.194	U	1000
Coprates	11° 46'9.38" S	67° 45' 3.76" W	62386	43639	28308	2.662	S	400
Coprates	10° 52' 26.26" S	68° 44' 01.83" W	29018	43296	20551	1.219	CF	150
Coprates	11° 14' 41.96" S	68° 7' 51.98" W	38039	59252	23476	5.093	S	N/A
Melas	10° 51' 7.03" S	70° 20' 10.39" W	67309	80461	29932		U	1000
Melas	9° 16' 19.13" S	71° 36' 58.24" W	12683	14153	10201		C	> 1500
Melas	9° 8' 51.20" S	72° 1' 36.40" W	32620	46254	27632		C	1000
Melas	8° 34' 42.50" S	71° 58' 26.84" W	28140	27650	32442		C	1200
Melas	7° 54' 28.20" S	71° 54' 50.04" W	23515	44857	32442		S	1000
Melas	12° 08' 26.25" S	74° 05' 00.67" W	21632	23192	15217		S	> 2000
Ophir	4° 23' 15.19" S	70° 34' 46.01" W	16266	34786	17277	7.470	CF	150
Ophir	3° 42' 43.97" S	71° 19' 4.41" W	24946	40357	22550	13.134	S	> 1000
Ophir	3° 28' 23.77" S	71° 38' 16.97" W	29363	50469	32393	5.484	S	100
Ius	7° 44' 21.65" S	79° 33' 33.10" W	28077	40763	24711		CF	N/A
Ius	7° 47' 16.42" S	79° 2' 59.70" W	48589	26795	31194	5.464	C	> 100
Ius	8° 37' 42.06" S	78° 1' 21.93" W	26294	40485	27958		C	100
Ius	8° 5' 35.68" S	77° 59' 7.29" W	57048	41898	35036		C	200
Ius	8° 15' 42.39" S	77° 37' 30.14" W	17220	35732	35036		C	> 1000
Ius	8° 00' 49.30" S	76° 48' 14.68" W	7319	14095	6905	6.105	U	N/A
Tithonium	5° 33' 02.26" S	87° 30' 00.44" W	14477	12004	9800	4.566	CF	1500
Candor	5° 16' 07.90" S	75° 19' 53.82" W	27146	36284	28261	4.021	CF	> 1600
Hebes	1° 35' 34.70" S	77° 08' 19.17" W	5213	7818	3401	8.113	CF	> 1000
Hebes	0°11' 44.42" S	76° 38' 28.38" W	17289	14507	5829	3.933	CF	N/A

[1]Surface slope angle measured for outer zones with CRISM coverage

[2]C= composite, S= superposed, CF= confined, U= unconfined

[3]Crater-counted estimates from Quantin et al. (2004b)

Watkins et al. Table 2. VM landslide outer zone morphometry

Chasma	*Latitude*	*Longitude*	*sp (m)*	*L (m)*
Candor	8° 10' 14.03" S	66° 23' 24.31" W	5296	9779
Candor	8° 12' 11.83" S	66° 35' 19.15" W	4554	9555
Coprates	11° 04' 21.92" S	67° 42' 41.09" W	3593	6605
Coprates	11° 14' 46.42" S	67° 22' 32.85" W	5350	11049
Coprates	13° 02' 03.54" S	62° 33' 28.04" W	2347	5021
Coprates	12° 53' 59.60" S	61° 18' 13.47" W	5534	17078
Coprates	13° 29' 46.34" S	65° 27' 51.23" W	6243	12143
Coprates	13° 15' 59.08" S	60° 25' 39.72" W	7547	17715
Coprates	13° 15' 54.45" S	60° 17' 39.60" W	4620	15955
Coprates	13° 36' 13.24" S	60° 28' 29.12" W	10312	19507
Coprates	14° 04' 55.27" S	55° 25' 39.09" W	3628	8975
Coprates	14° 24' 49.23" S	54° 02' 24.73" W	3543	6850
Coprates	14° 15' 28.57" S	53° 16' 23.48" W	1562	6294
Coprates	14° 19' 02.55" S	53° 04' 27.01" W	1139	3830
Ganges	7° 27' 00.19" S	51° 20' 57.44" W	3080	12258
Ganges	8° 20' 49.02" S	41° 35' 51.68" W	5232	9099
Ganges	7° 58' 29.88" S	41° 41' 10.58" W	3538	11562
Ganges	7° 55' 30.25" S	41° 36' 12.58" W	3972	6735
Hebes	1° 36' 24.42" S	77° 10' 05.82" W	5500	8517
Ius	6° 47' 20.90" S	89° 11' 43.83" W	5942	7411
Ius	7° 13' 52.72" S	82° 48' 28.99" W	3548	7808
Juventae	5° 01' 59.86" S	63° 09' 13.36" W	5064	18029
Melas	8° 02' 40.11" S	76° 48' 08.33" W	7247	15063
Melas	13° 19' 54.46" S	72° 02' 19.31" W	2675	7325
Ophir	3° 56' 58.01" S	74° 24' 02.80" W	2063	8872
Tithonium	4° 46' 28.05" S	82° 00' 02.27" W	5781	16216
Tithonium	4° 25' 52.83" S	85° 47' 50.71" W	1950	9164
Tithonium	4° 18' 39.28" S	87° 14' 25.81" W	2054	7692
Tithonium	4° 34' 24.50" S	87° 09' 44.89" W	3010	6865
Tithonium	4° 03' 23.02" S	87° 49' 20.95" W	4094	7277

Watkins et al. Table 3. Debris flow morphometry

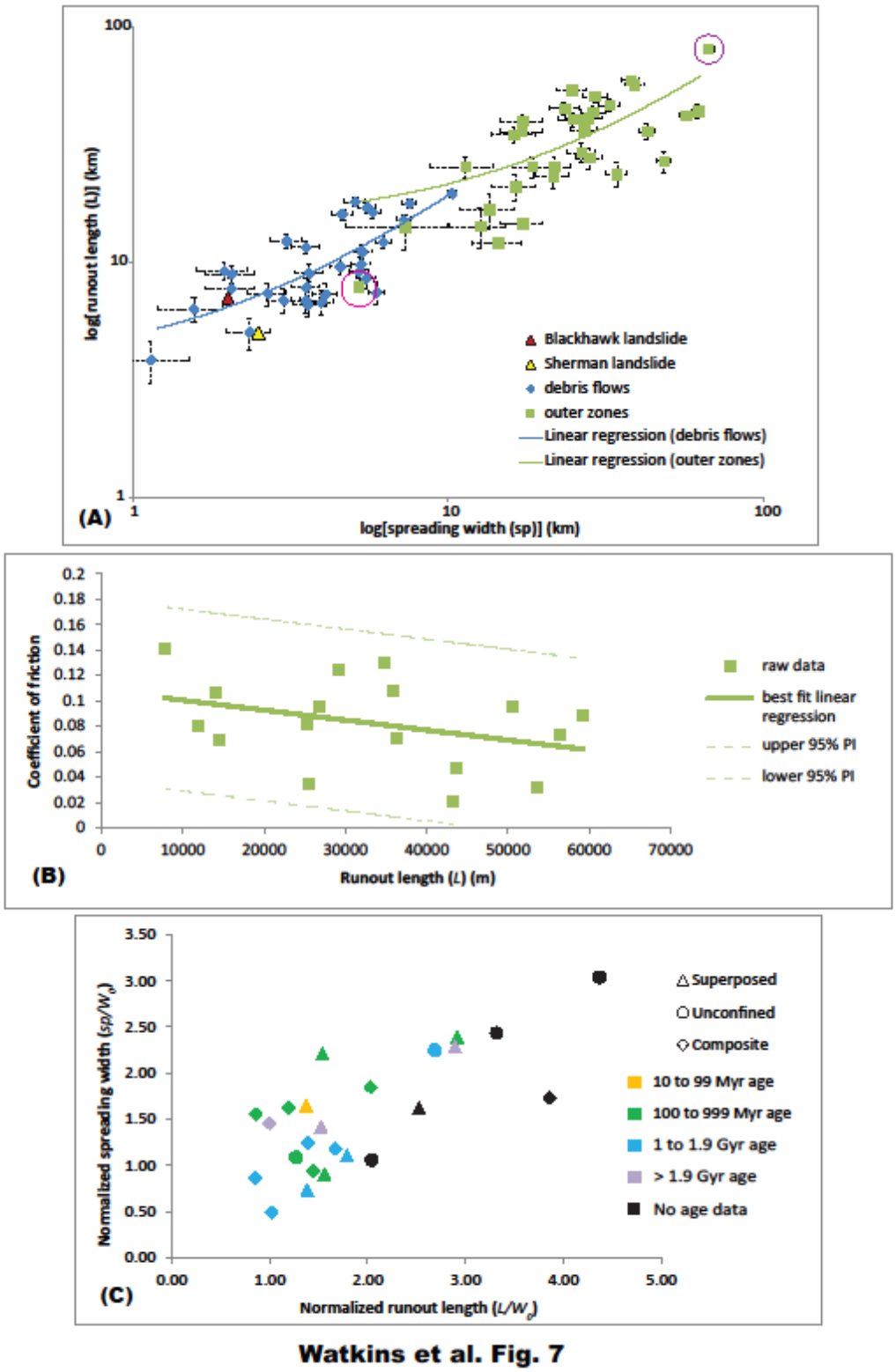

Watkins et al. Fig. 7

Figure 7. **Plots of VM landslide morphometry.** (A) Log-log plot of landslide runout length versus spreading width, for VM landslide outer zones and debris flows. Also plotted are the values for the Blackhawk landslide in California and the Sherman landslide in Alaska,

illustrating the exceptionally high mobility of VM long-runout landslides compared to terrestrial long-runout examples. Error bars represent standard error, defined as standard deviation of the sample mean. Also shown are linear regressions for VM outer zone and debris flow data. Pink circle is outer zone sample mobility minimum and is high mass; purple circle is outer zone sample mobility maximum and is low mass, demonstrating the variability within the broad mass dependence represented in the plot. (B) Plot of coefficient of friction, inferred as a function of measured surface slope angle, versus runout distance, which are inversely correlated. 95% prediction intervals for the linear regression (dashed lines) provide reasonable bounds for this trend. (C) Plot of landslide spreading normalized with breakaway width, a proxy for initial volume of the landslide mass, versus runout also normalized with breakaway width, as a function of age (Quantin et al., 2004b) and morphological classification (colors and symbols match those of Fig. 1). Note the lack of significant correlation, excluding age and subclass as contributing factors in unconfined landslide morphological variance.

landslide mass. However, the outer zone that exhibits minimum spreading and runout (pink circle in **Fig. 7A**) has an initial mass of 1.59 x 10^{16} kg (see table 1 in Quantin et al., 2004a), the second largest of the measured outer zones, whereas the outer zone that exhibits maximum spreading and runout (purple circle in **Fig. 7A**) has an initial mass of 9.405 x 10^{14} kg (see table 1 in Quantin et al., 2004a), in the smallest third of the measured outer zones. These observations exemplify the variability in the mass-mobility relationship, pointing to additional controlling factors.

The surface slope angle at the widest portion of the outer zone, an indication of basal friction, decreases with increasing runout length (**Fig. 7B**), potentially indicating a relationship between the variables (discussed in section 4.1). We normalize the landslide spreading width and the runout distance by the breakaway-scarp width (**Fig. 7C**). In doing so, we attempt to remove the effect of mass dependency in evaluating the relationship between the spreading width and other geometric parameters of the studied landslides (i.e., using the breakaway width as a proxy for landslide mass). In such a plot, we find that the normalized spreading width and runout distance remains linearly related (**Fig. 7C**). However, there is no systematic correlation of the data points with the crater-counted age of the landslides or their morphological classification (**Fig. 7C**). Regional slope also does not prove to be a control on aspect ratio, as all VM long-runout landslides occur along current regional slopes of < 3°.

3.3 Compositional Analysis

In previous spectral and structural analysis of a well-exposed VM long-runout landslide (Watkins et al., 2015), no hydrated minerals were detected in the source trough-wall rocks and inner zone, whereas a high-albedo stratigraphic unit in the basal layer of its toe was found to

contain hydrated minerals with absorption signatures consistent with the presence of hydrated silicates and Fe/Mg phyllosilicates. Structural relationships at the toe suggest that the basal layered units containing the hydrated silicates experienced sheared deformation during emplacement. This observation led to the hypothesis that hydrated silicates within the basal sliding zone may have facilitated long-runout landslide emplacement.

This work expands that of Watkins et al. (2015) by examining an additional 38 CRISM images, with 34 covering the outer zones of 14 regional landslides/landslide complexes. In addition, 2 of the 38 CRISM images cover a landslide inner zone and another two cover the transition regions between the inner and outer zones in two landslide systems. This study also examined 13 images covering trough floor materials surrounding the outer zones of 8 landslides, as well as 4 images covering a landslide breakaway scarp and proximal wall rocks.

Of the analyzed 14 landslide systems with outer-zone CRISM coverage, 8 landslides were found to exhibit the presence of hydrated silicate minerals in their long-runout sections (**Fig. 8**). Though the basal layers are largely unexposed, hydrated minerals are present in at least one example of each landslide classification. In western Ius Chasma, hydrated silicate and smectite were detected in the outer zone of a confined landslide (**Fig. 4**) in CRISM images 13EDE, 8FF0, and 88FC, consistent with the mapping of this unit as hydrated material by Roach et al. (2010). In central Ius Chasma, hydrated silicate and potential smectite, with a weak absorption at 2.3 μm, were detected in the outer zone of another confined landslide in CRISM images 1E247, 27E2, 905B, A396, C119, D740, and 18FD5, also consistent with the observations of Roach et al. (2010). In eastern Ius Chasma, Watkins et al. (2015) found that the Ius Labes composite landslide (**Fig. 5**) contains hydrated silicate and smectite. In eastern Coprates Chasma, kieserite,

a monohydrated sulfate, was detected in the outer zone of an unconfined landslide in CRISM image 93E3. In western Ganges Chasma, likely smectite with persistent but weak 1.4- and 1.9-

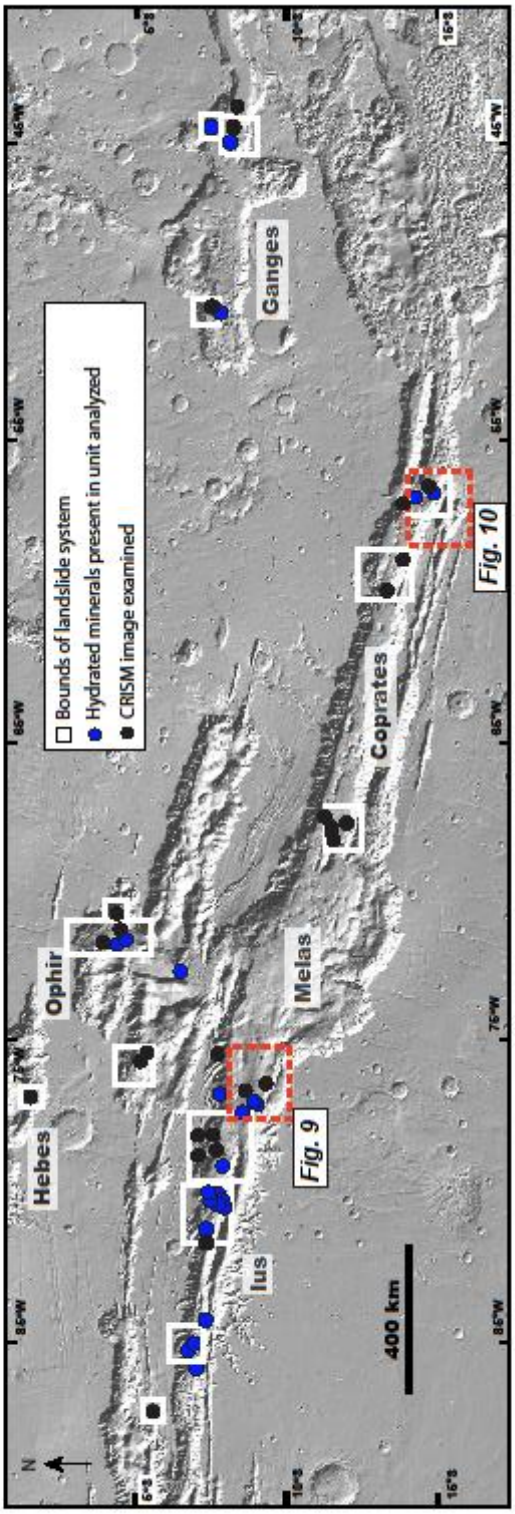

Figure 8. **Distribution of hydrated minerals associated with landslides in VM.** White boxes delineate individual landslide complexes. Blue circles within boxes indicate hydrated minerals

present in outer zone; blue circles outside of boxes indicate hydrated minerals present on the trough floor in the immediate vicinity. Black circles indicate landslide/trough-floor materials in CRISM image examined. Locations of Figs. 9 and 10 are also shown.

μm absorptions and a shoulder at 2.3 μm was detected in the outer zone of a composite landslide in CRISM image B48A. In northeastern Ganges Chasma, Fe/Mg smectite with a 1.9 μm absorption and an inflection at 2.3 μm was detected in the outer zone of a composite landslide in CRISM image 1693A. Hydrated minerals were also detected in the outer zones of a superposed landslide in southeastern Ganges Chasma (CRISM image 136CF; **Fig. 6**) and a composite landslide in Ophir Chasma (CRISM images A432 and 508A).

In order to understand whether the hydrated minerals in the studied landslides source from the wall rock or the trough floor, each of which could have implications for landslide initiation and/or transport mechanisms, the composition of the walls and floor in the immediate vicinity of the landslides was analyzed. CRISM data cover the trough floor surrounding 8 landslide outer zones. Upon compositional analysis of each of those trough floor regions, the presence of hydrated minerals was detected near 4 landslides (**Fig. 8**). At Ius Labes (see **Fig. 5**), a HiRISE anaglyph shows that the toe of the example hydrated landslide outer zone is juxtaposed over the clay-bearing broken-bed unit (*Abt*) of trough-floor deposits (**Fig. 9**). Previous identification of nontronite in trough floor units in this location by Weitz et al. (2015) corroborates this detection. Although most pristine breakaway and inner-zone material is obscured by talus and dust cover, hydrated silicate and Fe/Mg smectite (previously identified as Fe-rich allophane/opal and saponite in this location; Weitz et al., 2014) were detected in the upper layers of the inner zone of a superposed landslide in eastern Coprates Chasma, exposed along the intra-landslide boundary fault scarp and within a small channel (**Fig. 10**). This inner zone lies in an arcuate alcove above a steep scarp, below which the outer zone is emplaced on the trough floor. Fe/Mg smectite is exposed along this intra-landslide boundary scarp and on a knob formed by the tilted blocks.

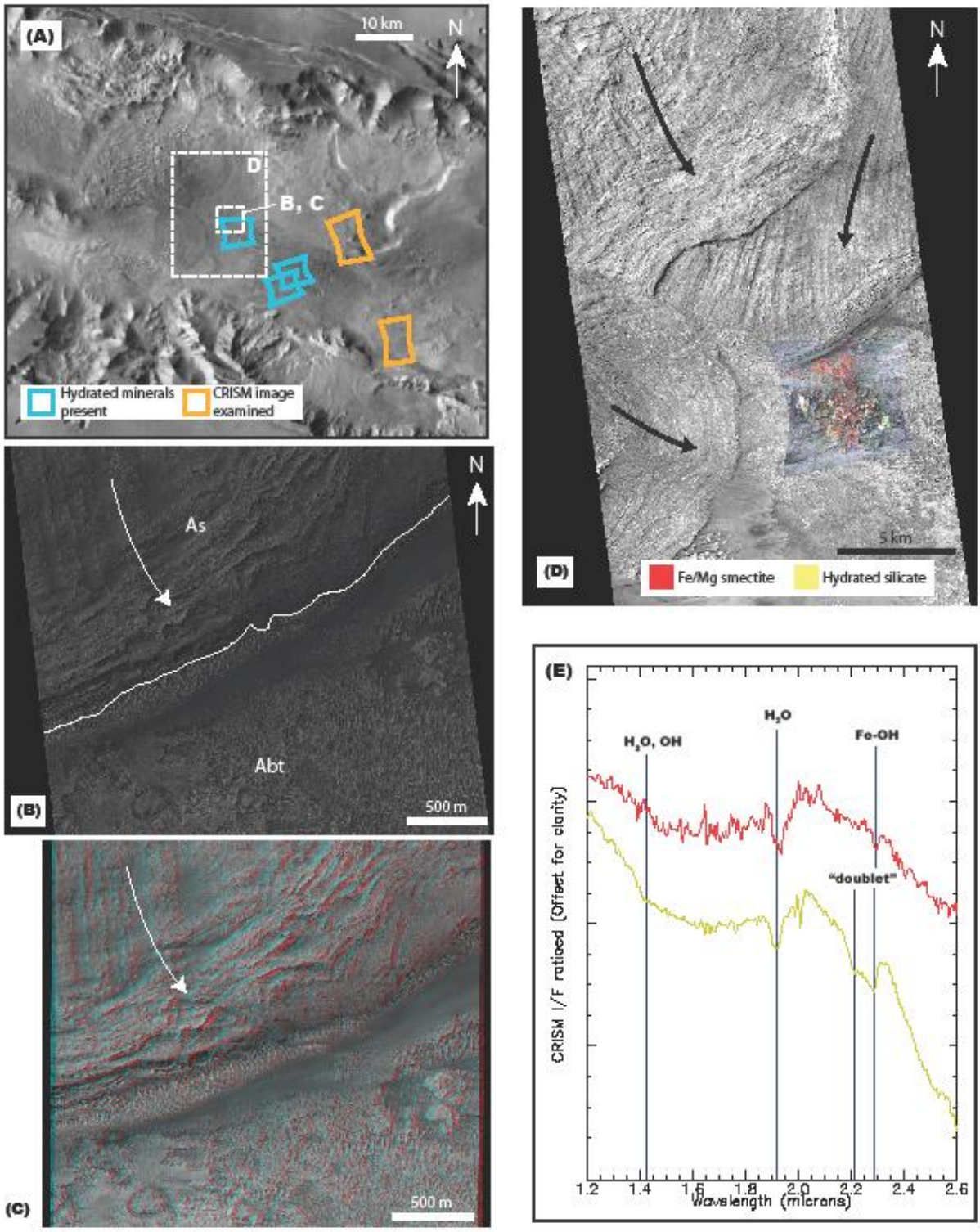

Watkins et al. Fig. 9

Figure 9. **Geologic relationships on western Melas Chasma floor.** (A) THEMIS mosaic showing the western Melas Chasma trough-floor context in the immediate vicinity of the Ius

Labes composite landslide mapped in Fig. 4 (see Fig. 8 for location), with the locations of CRISM images analyzed, as well as B, C, and D. Blue boxes indicate hydrated minerals present in trough-floor materials; orange boxes indicate CRISM image examined. (B) Map of geologic relationships in HiRISE image ESP_018941_1715. The contact between the landslide outer-zone toe (*As*) and the trough-floor unit (*Abt*) is clearly delineated. Arrow indicates landslide lobe transport direction. (C) HiRISE anaglyph (stereo pair ESP_018941_1715 and ESP_016739_1715) of contact in B, indicating that the floor units are stratigraphically lower than the outer zone. (D) Summary spectral parameters map of CRISM image FRT00016B12 highlighting the presence of hydrated minerals (R: BD1900R, G: Doub2200, B: D2300) overlain on CTX image G03_019218_1728_XN_07S078W. Arrows indicate transport direction of each lobe in the composite landslide. Fe/Mg smectites are red and hydrated silicate material is yellow with the stretches used. The landslide toe is visible in the top left corner of the CRISM image, and is unhydrated. The proximity and superposition of the landslide deposit to these hydrated-silicate-bearing trough-floor materials suggests clays may have played a key role in landslide emplacement. (E) Ratioed CRISM spectra for image FRT00016B12. The yellow spectrum corresponds to the yellow units in the summary parameters map; the red corresponds to the red units. Note the absorption at 1.9 μm, indicative of the presence of hydrated minerals.

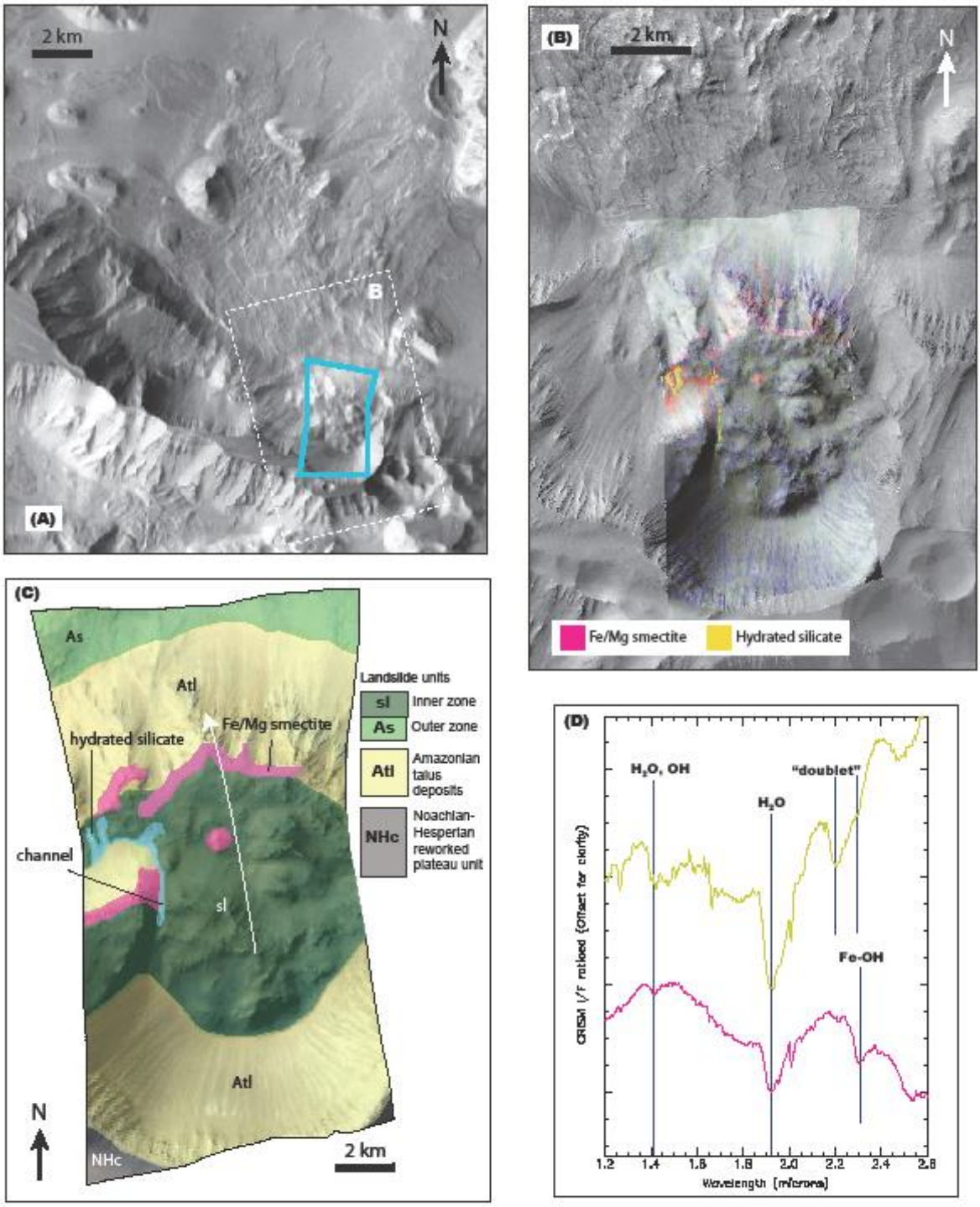

Watkins et al. Fig. 10

Figure 10. Compositional analysis of landslide inner zone. (A) THEMIS mosaic context map of landslide in Coprates Chasma (see Fig. 8 for location). Location of B is also shown; blue box outlines the location of CRISM image analyzed in B, C, and D. (B) Summary spectral parameter map of CRISM image HRL0000A8F6 highlighting the presence of hydrated minerals (R:

BD1900R, G: Doub2200, B: D2300) overlain on CTX image P18_008141_1647_XN_15S056W. Fe/Mg smectites are magenta and hydrated silicate material is yellow-green. Most of the landslide inner zone (lower half of parameter map) is unhydrated, but hydrated units are exposed near and along the intra-landslide boundary fault scarp (upper half of parameter map; see C for unit mapping). (C) Geomorphological mapping of landslide units covered by CRISM image A8F6 based on photogeologic analysis of corresponding satellite images. Arrow indicates landslide transport direction. Hydrated silicate is mapped in blue; Fe/Mg smectite in pink. (D) Ratioed CRISM spectra for image A8F6. The yellow spectra corresponds to the yellow-green, hydrated-silicate units in the summary parameters maps; the magenta corresponds to the magenta, Fe-Mg-phyllosilicate units. Note the absorption at 1.9 μm, indicative of the presence of hydrated minerals.

Hydrated silicate is exposed within a small surficial channel cut into the ridges of the inner zone (**Fig. 10C**).

To determine whether composition affects the parameters examined in morphometric analyses, runout length normalized with spreading is plotted against breakaway width and categorized by the detection of clay minerals in landslide outer zones. Outer zones with hydrated minerals may run out further at smaller initial volumes and spread laterally more at larger initial volumes as compared to those without hydrated mineral detections (**Fig. 11**). However, these trends do not reach statistical significance in a Mann-Whitney U test. This variability could be partially due to low n values (i.e., sample size) as a result of limitations in CRISM data coverage; further data may yet reveal statistically significant variability.

Inherent in the statistics of the hydrated mineral distribution is the irregular exposure of outer-zone basal layers, pristine trough-floor deposits, and source wall rock at the surface for unobstructed detection by CRISM. The exposure of basal material depends on the relative proportion of basal material and on the circumstances of the entrainment and transport process (Hungr and Evans, 2004). As a result, the lack of detection of clay minerals in some locations may, in addition to their actual absence or insufficient abundance for orbital detection, be explained by dust or talus cover or burial of entrained materials by overriding units (see **Fig. 14C**) and CRISM coverage of landslide and trough floor surfaces. For example, ~20 wt. % clay in the Yellowknife Bay region of Gale crater's floor (e.g., Vaniman et al., 2014) was not detected in CRISM data due to dust cover. Thus, the hydrated minerals detected are a lower bound on the hydrated minerals actually present.

4. Discussion

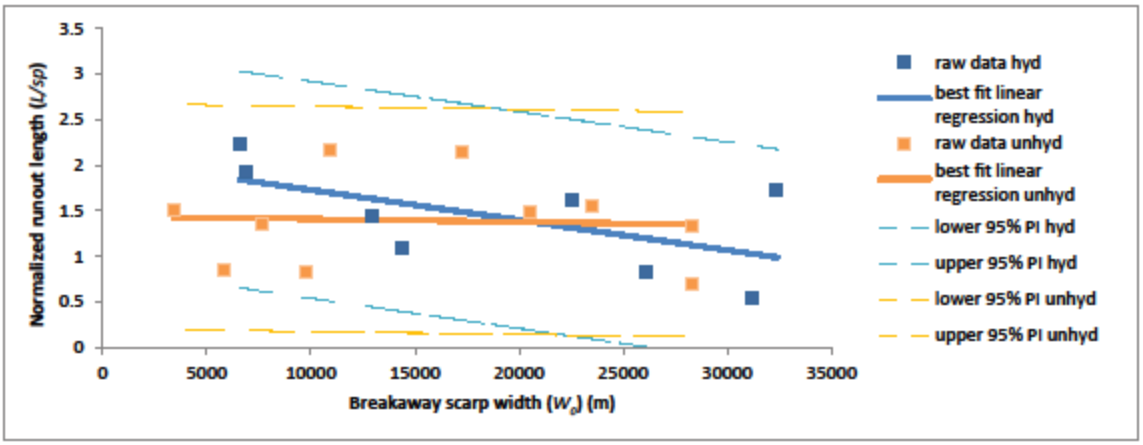

Watkins et al. Fig. 11

Figure 11. **VM outer zone mobility by hydration.** Plot of runout length normalized with spreading versus breakaway width categorized by the detection of clay minerals in landslide outer zones. The equation for the linear regression for unhydrated outer zones is $y = -3*10^{-6}x + 1.4411$, with an R^2 value of 0.0034. The equation for hydrated outer zones is $y = -3*10^{-5}x + 2.0603$, and $R^2 = 0.3675$. 95% prediction intervals for the linear regressions (dashed lines) provide bounds for these trends. Hydrated outer zones appear to largely exhibit longer runout and increased lateral spreading as compared to unhydrated outer zones.

In this study, we divide VM landslides into four subclasses based on the boundary conditions of landslide emplacement, and find that the characteristic two-zone morphological division persists throughout VM despite variability in subclass, age, and location within the canyon. Our morphometric analyses of VM landslides indicate that the outer-zone spreading width and landslide mass inferred from the width of the breakaway zone increase with runout distance, and the lateral taper angle of the outer-zone lobes measured in the direction perpendicular to that of landslide transport decreases with increasing outer-zone runout distance. Our CRISM compositional analyses show that hydrated silicates occur commonly, although not always, in landslide outer zones and trough-floor regions surrounding outer zones. We also observe a modest increase in runout and lateral spreading of outer zones with hydrated mineral detections compared to those without, and detect hydrated minerals in one landslide inner zone. Below we discuss the implications of these findings and place them into the context of several end-member models for the emplacement mechanisms of VM landslides.

4.1 Improved Estimate of Coefficient of Friction Show Low Basal Friction of Outer Zones

Early workers quantified landslide geometry using primarily the vertical drop height (h) vs. transport distance (L) ratio (h/L), which is in turn used as a proxy for estimating the coefficient of basal friction (e.g., McEwen, 1989; Quantin et al., 2004a; Lajeunesse et al., 2006). This friction estimate is based on the assumption that gravitational potential energy ($E_g = mgh$) of a landslide mass (m) is completely consumed by basal shearing during landslide transport ($E_f = \mu mgL$) where μ is the effective coefficient of basal friction, g is gravitational acceleration, and L is the landslide transport distance (Iverson, 1997). These simplified physical relationships require that $\mu = h/L$, which is incomplete as kinetic energy must have also contributed to

landslide motion at high speed (Di Toro et al., 2004), basal friction causes heating, and finally mass movement may involve turbulent flow rather than simple frictional sliding (e.g., Harrison and Grimm, 2003). We expand on the early work by exploring and quantifying more geometric attributes of a landslide system, and instead estimate the VM landslide outer-zone coefficient of basal friction from measured surface slope angle in the lateral spreading zone, a more accurate proxy. This coefficient of friction is an effective value that includes any effect of pore-fluid pressure and is more analogous to kinetic friction.

The validity of this inferred value is supported by its inversely proportional relationship with runout distance (**Fig. 7B**). Overall, the inferred coefficients of basal friction estimated for VM landslide outer zones using the surface slope angle range from 0.02 to 0.14. Variability in basal coefficient of friction may account for the observed substantial variance in mass dependency for VM landslide mobility. Relative to values previously determined with different methods, our coefficients of friction are < ⅓ (on average) that determined by recent analysis of high resolution imagery (Brunetti et al., 2014), and correspond to the lowest estimated values for terrestrial subaerial long-runout landslides. The coefficient of basal friction is estimated to be ~0.105 for the 2014 landslide near Oso, Washington, which is composed of water-saturated sediments at its base (Iverson et al., 2015), ~0.31 for the Elm landslide in the Alps (Hsü , 1975), ~0.13 for the Blackhawk landslide in California (Johnson, 1978), ~0.22 for the Sherman landslide in Alaska (McSaveney, 1978), ~0.011 for the Storegga submarine landslide in Norway (Hampton et al., 1996), and ~0.055 for the clay-rich (10-16%) Teteltzingo lahar at Citlaltépetl volcano, Mexico (Carrasco-Núñez et al., 1993).

The low coefficients of friction values derived from VM landslide lateral spreading zones are determined independent of mass. This implies that large initial volumes nor heights of initiation

(up to 7 km in VM) do not alone explain runout distances. We now consider the morphological properties and emplacement mechanisms of the above and other earth and planetary analogs to the VM landslides in order to further constrain the mechanism that reduces the coefficient of friction during transport.

4.2 Comparison of landslide attributes to terrestrial analogs

As described in section 3.2 and illustrated in **Fig. 7A,** no perfect analog for VM long-runout landslides exists based on a comparison of characteristic morphometric parameters. In addition, the mechanism(s) of long-runout landslide mobility even in terrestrial settings have remained elusive (e.g., Hungr, 1995; Melosh, 1987; Shreve, 1968a; Hsü, 1975; McSaveney, 1978). However, insights into VM landslide emplacement mechanisms can be gained from study of relevant aspects of the available long-runout analogs.

4.2.1 Kinematic analogs

The resemblance of VM long-runout landslide morphological features to those of rampart crater ejecta deposits on the VM plateau (Barnouin-Jha et al., 2005) suggests that comparison may provide insight into landslide evolution. These lobate, fluidized ejecta blankets exhibit grooved morphology in their distal portions that resemble that of VM landslide outer zones as well as a terraced structure, indicative of outward slumping of the rim region, resembling the slump blocks and scarp-like features of VM landslide inner zones (Barnouin-Jha et al., 2005). Around the craters, distal ejecta are inferred to be emplaced more rapidly than the near-rim ejecta, both of which can be explained by a basal sliding mechanism (Barnouin-Jha et al., 2005). Like VM outer zones, linear, longitudinal grooves parallel to the direction of transport

qualitatively indicate rapid emplacement (Lucchitta, 1979; McEwen et al., 1989, Brunetti et al., 2014; De Blasio, 2011; Dufresne and Davies, 2009). Rampart crater distal ejecta have initial sliding velocities of up to ~70 m/s for an analogous volume of displaced material (Weiss and Head, 2014). Emplacement speeds of up to 132 m/s and 118 m/s have been calculated for VM long-runout landslide outer zones in Melas and Ophir Chasmata, respectively (Mazzanti et al., 2016). When scaled for initial relief, these VM outer-zone emplacement speeds are comparable to those of distal ejecta and may indicate that VM long-runout landslide evolution similarly includes slower emplacement of the inner zone following initiation, and subsequent rapid emplacement of the outer zone.

4.2.2 Extraterrestrial landslides

Long-runout landslides observed on Venus, the Moon, Io, Phobos, Callisto, and Vesta have morphologic characteristics that resemble those of VM landslides. Although landslides on Venus are smaller than those in VM, they share a theater-like headscarp, a hummocky surface near the apex, and a wide deposit at the toe (Malin, 1992). Lunar examples lack obvious breakaway scarps and inner zones, but do exhibit faint longitudinal ridges on their thin depositional lobes (Howard, 1973). A prominent landslide deposit on Io was derived from an arcuate escarpment and is similarly ridged; however, it also lacks an inner zone and is much thicker than its VM counterparts (Schenk and Bulmer, 1998). Landslides observed on the floors of craters on Phobos source along the crater rim and are characterized by hummocky relief but lack distinct inner-zone slump blocks and emplacement-related outer-zone grooves (Shingareva and Kuzmin, 2001). On Callisto and Vesta, lobate deposits resemble VM outer zones (though they are devoid of grooves) and slump-like deposits resemble VM inner zones, but the two types

do not occur together as in VM (Chuang and Greeley, 2000; Krohn et al., 2014). Each of these extraterrestrial slides was likely emplaced without the active involvement of fluids.

4.2.3 Landslides with multiple lobes and longitudinal grooves

Several terrestrial long-runout morphological analogs may also provide insight into VM landslide outer zone emplacement. First, the Mount La Perouse rock avalanche that occurred in Alaska in 2014 provides an example of the emplacement of multiple lobes within a singular event, as is common in terrestrial debris flows (Iverson, 1997) and interpreted to be the case for composite landslides in VM (**Fig. 12A**). Ice and snow are evident within the exposed toe of the long-runout avalanche (**Fig. 12B**), suggesting that its transport was facilitated by the entrainment of low-friction ice and snow as it was emplaced. The Sherman landslide was similarly transported on top of a glacier (Shreve, 1966). Both avalanches exhibit a grooved morphology resembling that of VM landslide outer zones (**Fig. 12A**). However, the source breakaway scarps of these features are shallow and lack tilted blocks characteristic of VM inner zones.

4.2.4 Landslides containing clay-rich material

While it lacks distinct longitudinal grooves, the Blackhawk landslide may demonstrate the potential influence of clay-rich material in long-distance landslide transport, as altered gneiss breccia and sandy mudstone are exposed within its long-runout portion (Shreve, 1968b; Johnson, 1978). Alternatively, transport of the Blackhawk landslide and the Elm landslide, also devoid of radial grooves as well as a deep-seated breakaway scarp, has been attributed to trapped air in their basal sliding zones (Shreve, 1968b). Operation of such a mechanism on Mars may require a

Watkins et al. Fig. 12

Figure 12. **Mount La Perouse rock avalanche, Alaska**. (A) Spread of the landslide toe and emplacement of multiple long-runout lobes within the single event. Note also the grooved morphology which resembles that of VM long-runout landslides, implying a similar transport mechanism. Location of B also shown. (Photo used with permission from Drake Olson.) (B)

Constituent materials at the landslide toe, consisting of ice and snow, suggesting that the landslide entrained a large amount of snow and ice as it travelled downslope, and providing one possible kinematic analog for VM landslide outer-zone transport. (Photo used with permission from Drake Olson.)

much denser atmosphere in its recent history (~50 Ma, the youngest VM landslides; see Quantin et al., 2004b) (Lucchitta, 1978).

The Teteltzingo lahar on the flank of the Citlaltépetl volcano also exhibits the influence of clay-rich material on landslide mobility. The presence of glacial ice and a hydrothermal system within the Citlaltépetl volcano is suggested to have produced water-saturated, hydrothermally altered, smectite-rich rock that flowed down the steep flank as a debris avalanche (Carrasco-Núñez et al., 1993). The Teteltzingo lahar's debris-flow-like morphology (e.g., incised proximal channel and flat distal deposit), though, is distinct from the amphitheater breakaway scarps and grooved outer zones characteristic of VM landslides.

4.2.5 Landslides with basal clay layers

The Portuguese Bend landslide in Palos Verdes, CA (**Fig. 13**) is a long-runout earthflow that was emplaced on bentonite-lubricated slip planes in which fine-grained debris and bentonite underwent plastic flow. This clay (altered tuff) is rich in the smectite montmorillonite and is highly thixotropic, causing a dramatic reduction of shear strength and viscosity upon shear stress (Kerr and Drew, 1967). Terrestrial thixotropic clays commonly form long-runout earthflows involving saturated fine-grained slope material that liquefies and runs out downslope with substantial internal deformation (Baum et al., 2003). Unlike VM landslides, it was emplaced slowly rather than quickly and also lacks longitudinal grooves.

The Oso and Storegga landslides exhibit rotational slump blocks at their heads and a debris apron resembling that of a VM outer zone, though longitudinal grooves are not preserved. In the case of the Oso landslide, this debris apron closely resembles a confined VM outer zone. In the case of the submarine Storegga landslide, it resembles that of a composite VM outer zone with

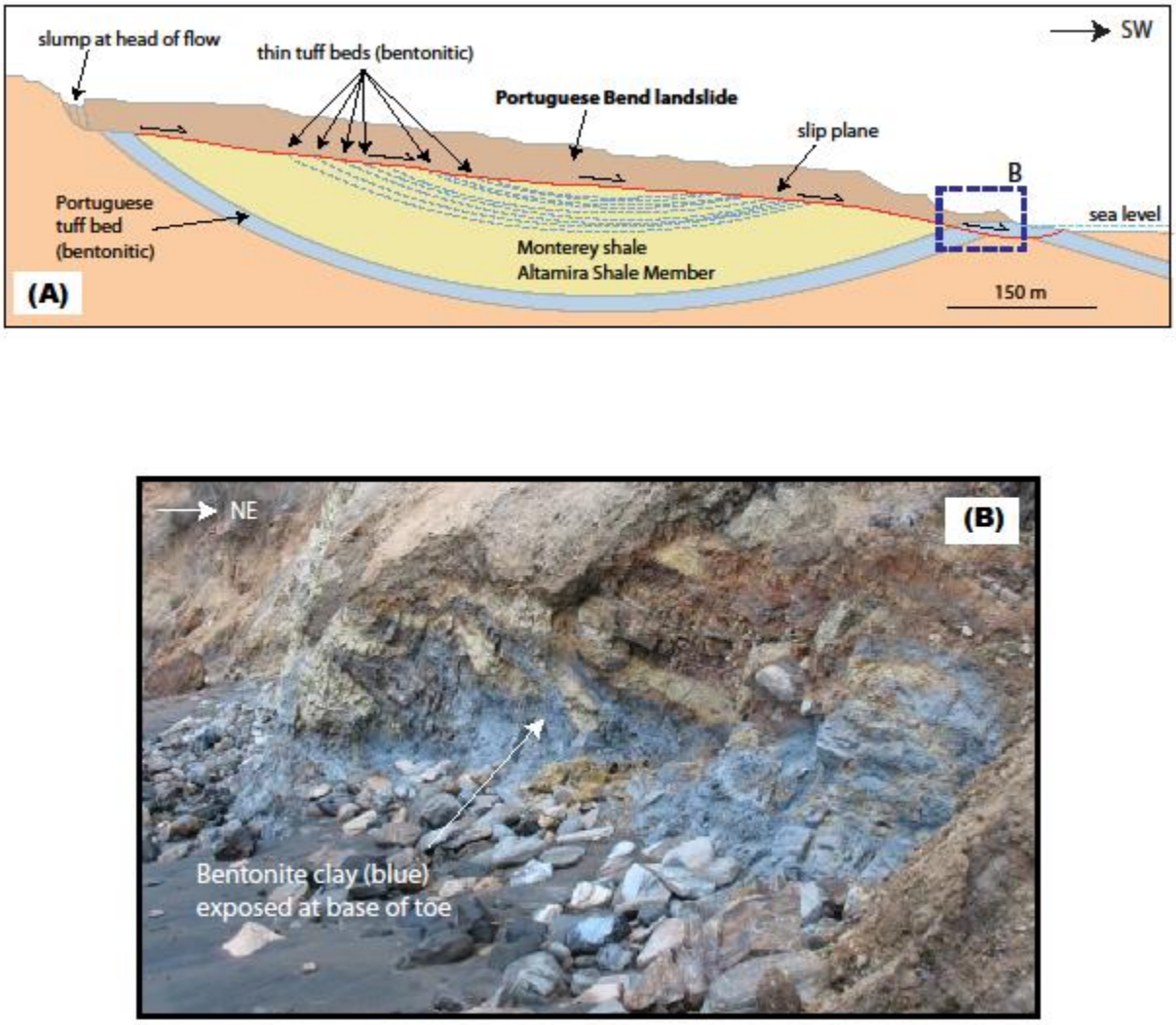

Figure 13. **Portuguese Bend landslide, California.** (A) True-scale schematic cross section, showing features of the slide (after Kerr and Drew, 1967). Note the clay-rich (altered tuff) layers along the slip surface, which experienced a significant loss in shear strength upon absorption of water and lubricated the base of the earthflow during emplacement. This example provides a possible mechanistic analog for VM landslide outer zone emplacement, which may have involved thixotropic flow and basal lubrication by smectite clay to form earthflow long runout. (B) Bentonite clay (blue) exposed at the base of the Portuguese Bend landslide toe, revealing its contribution to lubricated basal slip (after Douglas, 2011).

multiple lobes forming during one main event (Haflidason et al., 2005). It has been proposed that both of these slides were emplaced as a result of liquefaction of basal clays, facilitated by groundwater saturation of the glaciolacustrine silt and clay composing the basal layer of the Oso landslide (Iverson et al., 2015) and hydroplaning and turbidity currents in combination with the remolded marine/glaciomarine clays at the base of the Storegga landslide (Bryn et al., 2005; Kvalstad et al., 2005). Though no analog is morphologically identical, several of these low-coefficient-of-friction slides are partial analogs. This enables us to test the efficacy of these emplacement models for VM landslides.

4.3 Potential Emplacement Mechanisms

Synthesis of the local and surrounding regional geologic context of VM long-runout landslides suggests that hydrated outer zones are not anomalous within the canyon. Detection of hydrated minerals in over half of VM landslide outer zones implies a possible relationship between outer-zone morphologies and the presence of clay minerals and other hydrated silicates. Though compositional data covering the basal layer of every landslide is not available for examination, hydrated materials may be present below most of the landslides based on the observed occurrence in those that are well-exposed, as well as projection of documented regional geology, which includes widespread hydrated silicates on the VM trough floor (Roach et al., 2010; Flahaut et al., 2010; Thollot et al., 2012; Weitz et al., 2011; 2012; 2015; Williams and Weitz, 2014). The clay-bearing trough-floor deposits pre-date emplacement of the landslides based on contextual relationships (Murchie et al., 2009a; Roach et al., 2010). Where the outer-zone basal sliding layer is singularly well-exposed in Ius Chasma, geologic mapping of Ius Labes by Watkins et al. (2015) further indicates both that deposition of hydrated minerals

(detected in CRISM image B939) preceded landslide emplacement and that these hydrated trough-floor materials could have been incorporated into outer zones during transport.

The question thus arises: do clays play a role in long-distance VM landslide transport? Morphometric relationships exclude age, classification, and regional slope as key contributing factors in unconfined outer zone morphological variance. The low regional slope values observed for the trough floor indicate a flat environment as is required for lateral spreads. Controlling for mass, the data show that landslides with hydrated materials may run out slightly less because they are spreading more (**Fig. 11**). The relationship is not statistically significant; however, it is suggestive that clays may serve as basal lubrication, lowering the coefficient of friction. This leads us to independently evaluate each mechanism of emplacement proposed in the previous section in light of these observations and this hypothesis.

4.3.1 Dry emplacement mechanisms

Despite the observed correlation of clays with VM landslide outer zones, it cannot be ruled out that clay minerals could play a negligible role in VM landslide transport. Dry dynamic weakening mechanisms (e.g., mechanical or acoustic fluidization; Davies, 1982; Collins and Melosh, 2003) or granular flow of entrained sediment or rock fragments (e.g. Mangeney et al., 2010; Johnson & Campbell, 2017) may explain the apparent reduction in coefficient of friction by a temporary lowering of the normal stress between landslide fragments.

Volumetric and topographic effects (Lucas et al., 2011; 2014; Soukhovitskaya and Manga, 2006; Lajeunesse et al., 2006; Johnson & Campbell, 2017) or friction-induced shear-zone melting (De Blasio and Elverhøi, 2008; Weidinger and Korup, 2009; Erismann, 1979) may also facilitate long-distance landslide transport under the dry condition. Given that hydrated

minerals and VM landslide outer zone mobility are only weakly correlated (see **Fig. 11**), it is plausible that clay minerals are not present in abundances required for lubricating effects, that they are present in sufficient quantities but not hydrated/swelled so as to cause lubrication, and/or some portion of the clay minerals observed are surficial deposits rather than entrained in the basal layer. If mapping of the unit relationships as presented in section 3 is incorrect, alteration to form the clay minerals could have occurred after landslide emplacement and clays might instead indicate longer term water activity. These relationships can be tested by future studies as orbital data acquisition continues.

Dynamic, analytical, and experimental modeling of VM landslide geometry performed so far has produced contradictory results for dry VM landslide emplacement mechanisms. Dynamic numerical modeling, which computes the initial mass profile and time-varying shape of a given runout path, of a simulated dry (acoustic fluidization) landslide rheology does not match well the cross-sectional geometry of most VM landslides (Harrison and Grimm, 2003). In contrast, statistical comparison of VM landslide geometry (specifically, the power-law relationship between volume and runout distance) with that of terrestrial landslides (Soukhovitskaya and Manga, 2006; Johnson & Campbell, 2017) and extrapolation of laboratory-scale experimental studies of dry granular flows to VM landslides (Lajeunesse et al., 2006) suggest that VM landslide emplacement was predominantly dry. Basal melt generation through frictional heating may have facilitated VM landslide transport along a layer of molten rock as shown in a numerical model by De Blasio and Elverhøi (2008), but further experimental testing at high shear rates and pressures is required to constrain its viability on a regional scale.

4.3.2 Ice-facilitated emplacement mechanisms

Lubrication of VM landslides as a result of emplacement on ice has been previously proposed largely based on morphological analogy with terrestrial long-runout examples such as the Sherman landslide (see section 4.2.3) (Lucchitta, 1987; De Blasio, 2011). The prevalence of highly-mobile rampart-crater ejecta around Valles Marineris (though they are rare along the trough floor) has been interpreted to be indicative of the presence of ground ice (Peulvast et al., 2001), and morphometric similarities with VM landslide deposits (described in section 4.2.1) may also suggest that ice played a role in VM landslide emplacement. In this scenario, the observed clay minerals may have formed prior to landsliding and been entrained with ice during landslide transport (perhaps even formed within the ice; Niles and Michalski, 2009).

The coefficient of friction for solid ice can be sufficiently low for lubrication at high sliding velocities and temperatures warmer than -30°C (Singer et al., 2012). The characteristic total energy dissipation per unit mass at the beginning of a slide event, given as gh by Iverson (1997), equates for h = 6.1 km on average in VM (Quantin et al., 2004a) to an average of 23 kJ/kg of frictional heat. Given an average Mars surface temperature of -55°C, and an average rise in temperature due to this frictional dissipation along the sliding surface at the base of a typical (basaltic) VM slide of about 27°C, as well as the rapid emplacement speeds referred to in section 4.2.1, these surfaces could have moved into the slippery regime, facilitating long-distance transport.

4.3.3 Wet emplacement mechanisms

High pore water pressure in the basal sliding zones may have reduced the effective frictional coefficient and facilitated the long-distance transport of VM landslides (e.g., Lucchitta, 1987; Harrison and Grimm, 2003). Within this hypothesis, saturation or near-saturation of

sedimentary rocks or sediments at the base would reduce friction to the range of lower-bound values determined for VM landslides in this work. Liquefaction of these sediments, which induces penetrative deformation and substantial reduction in strength (Lowe, 1975), is consistent with the observed morphology, including the longitudinal grooves as well as prevalent soft-sediment deformation in trough-floor deposits in the region (Metz et al., 2010).

There are several possible sources for the water implied by this mechanism. First, it has been hypothesized that Valles Marineris was once filled by a lake(s) (Lucchitta, 2010; Harrison and Chapman, 2008; Warner et al., 2013). Conceivable within this setting is the possibility of subaqueous VM landslide emplacement by a mechanism similar to that of the Storegga landslide. If the trough system were filled (3.6×10^6 km^3; Lucchitta et al., 1994), though, this would require perhaps unreasonable amounts of standing water at the Mars equator, continuously or episodically over billions of years, including the last billion. Moreover, the deformational features that have been observed in VM and attributed to landsliding are much larger-scale than those produced by terrestrial submarine landslides (Metz et al., 2010). The presence of shallower lakes might still be plausible, but coastal terrestrial landslides produce much more extensive deformation directly adjacent to their toes (Frey-Martínez et al., 2006), not observed in VM, and do not exhibit longitudinal grooves (e.g., Forshee and Yin, 1995). The persistent preservation of these grooves in VM long-runout landslides, especially on the surface of the underlying lobe of a superposed landslide (e.g**., Figs. 3 and 6**), suggests that they experienced less disturbance during emplacement than would be expected as a result of lubrication by a shallow water layer. Another potential water source is the percolation of groundwater in VM, as was the case for the Oso landslide (Iverson et al., 2015).

Ice/snow may have also served as a wetting mechanism via melting of entrained ice/snow by high basal shear stresses in the basal layer. This meltwater could have also participated in the clay-formation process, a relationship exemplified by the Teteltzingo lahar. An issue with this model is that the average 23 kJ/kg of frictionally dissipated energy produced during landslide emplacement can move ice into the slippery regime (section 4.3.2) but is unlikely to be sufficient to melt ice for lubrication. Even for ice at 0°C, 334 kJ/kg is required for melting (Harrison and Grimm, 2003), necessitating more than 10 times the average supply, even if most slide energy was partitioned to friction and not transport. Basal heating to melt ice is thus unlikely to be the driving mechanism for wet lubrication of VM landslide long-distance transport.

The available volume of water is critical in dictating the viability of various mechanisms for water-induced friction reduction, given that the effective coefficient of friction of Coulomb materials under constant stress decreases with increasing pore fluid pressure (e.g., Legros, 2002; Iverson et al., 1997; Al-Shayea, 2001; Morrow et al., 2000). A special case of the wet emplacement mechanism is that of thixotropic behavior (swelling and complete loss of strength) of clays under shear. Atterberg liquid limit values for the transition to viscous flow, obtained for bentonite exposed at the toe of the Portuguese Bend landslide, range from 80-102% water content relative to dry mass (Watry and Ehlig, 1995). Assuming this minimum liquid limit of 80%, the minimum volume of pore water required to produce thixotropic clays at the base of a single average VM outer zone would be ~200 km^3. While numerical models have predicted comparable volumes of groundwater in VM in the Noachian and Hesperian (Andrews-Hanna and Phillips, 2007), it is unclear whether sufficiently large volumes were present in the groundwater table through the Late Amazonian when the youngest landslides were emplaced. As discussed in

section 4.3.1, in the alternative scenario where the observed clays formed post-emplacement, clays could be indicative of the sustained presence of water.

Within the liquefied basal clay scenario, there are two possibilities for the source of the liquefied clays. One possibility is that the hydrated minerals formed as a result of preferential alteration along a fractured fault zone (e.g., Viviano-Beck and Murchie, 2014) and were present in the VM source wall rock prior to landsliding (**Figs. 14A and 14B**). However, a fault-zone sourced self-lubrication model is largely inconsistent with regional observations of VM landslide source regions, which rarely show clay minerals to the extent they have been imaged with CRISM. Another possibility is, as described in the basalt clay-lubrication model of Watkins et al. (2015) (**Fig. 14C**), clay minerals regionally present in proximal trough-floor deposits prior to VM landslide occurrence (e.g., Roach et al., 2010) are entrained into the turbulent, granular flow in the basal layers of overriding outer zones and lubricate their long-distance transport. The observed presence of hydrated minerals in the overriding outer zone of the superposed landslide in Ganges Chasma (**Fig. 6B**) is also consistent with the entrainment of clay-bearing material from the underlying lobe.

The sustained accumulation of clay minerals on the VM trough floor may have been induced by: (1) erosion of proximal wall rock containing hydrated minerals, likely as a result of ongoing activity along trough-bounding faults associated with the extensional opening of the canyon; (2) erosion and aeolian redeposition of clay-bearing sediment from the plateau above the trough rims (e.g., Le Deit et al., 2012), and (3) in-situ weathering and alteration of trough-floor materials (Roach et al., 2010). Given that smectites formed in ancient equatorial Mars can remain in a hydrated state in present-day surface conditions (Bish et al., 2003; Vaniman et al., 2014), the clay-lubrication model requires only that these processes take place at any point prior

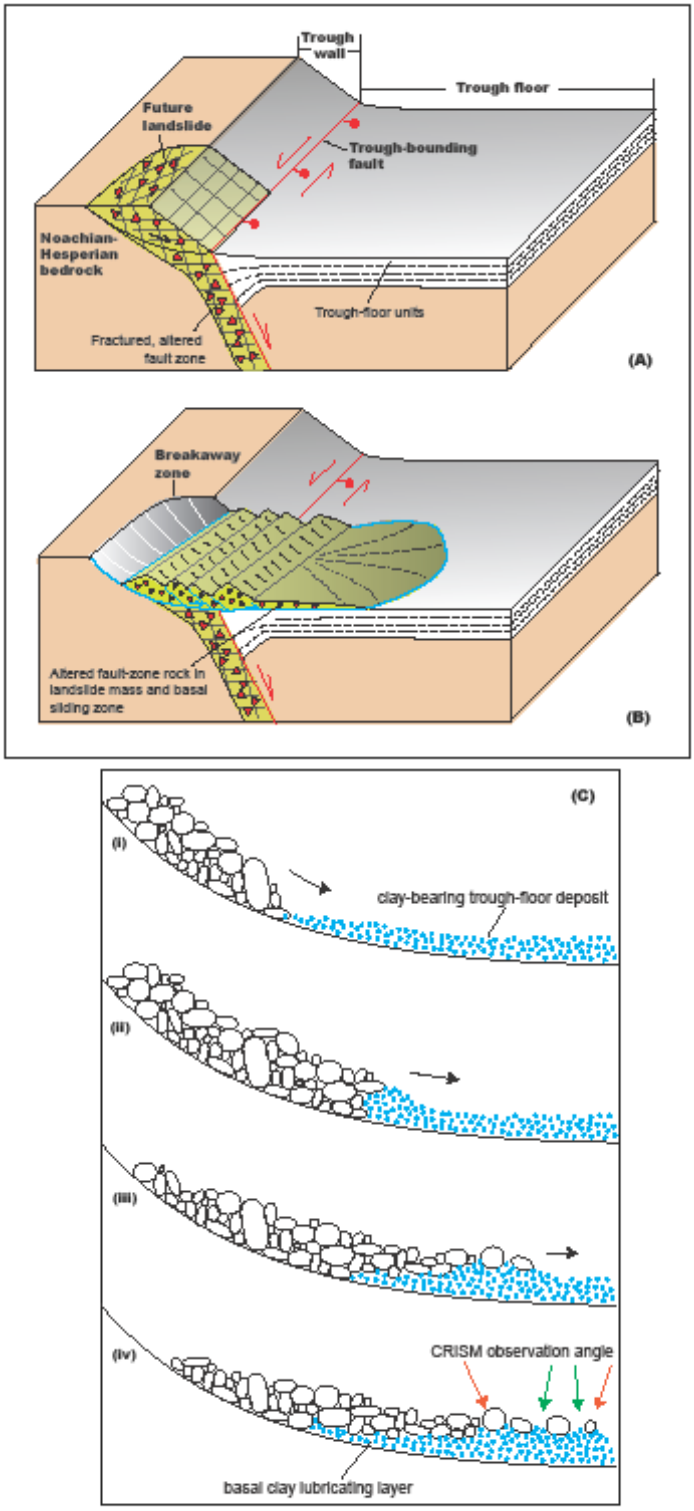

Figure 14. **Models for lubrication by liquefied basal layer**. (A) Self-lubrication model assumes pre-landsliding initial condition of fault-zone rocks that have been locally altered and

exhumed, and (B) landslide emplacement as a result of collapse along a breakaway scarp and transport through self-lubrication of altered fault-zone rocks. Based on the compositional data (as detailed further in the Discussion text), this model is not favored. (C) Clay-lubrication model (Watkins et al., 2015; after Hungr and Evans, 2004), consistent with the compositional data (as detailed in the Discussion text): (i) Landslide mass moves downslope and approaches clay-bearing trough-floor deposit, (ii) Collision-induced liquefaction, partial displacement, and overriding of the clay sediments, (iii) Entrainment of low-friction hydrated-silicate-bearing material into basal layer, (iv) Sliding zone is lubricated by liquefied clay layer; Overriding coarser-grained material irregularly obscures basal clay layer from detection by CRISM (green arrows indicate clay-bearing material exposed for CRISM detection; red arrows, obscuration).

to landslide occurrence. This is consistent with climate-independent emplacement as implied by the diverse range of VM landslide surface ages.

5. Conclusions

Quantitative morphologic investigation of landslides in VM reveals a characteristic two-zone morphology that persists despite emplacement age, subclass, and location. Estimated minimum coefficients of basal friction, calculated based on measured surface slope angle, were found to decrease with increasing runout length and spreading width, thus implying basal friction may account for observed variation in the mass dependency of VM landslide outer-zone runout distance and lateral spreading. Calculated effective coefficients of friction of 0.02 to 0.14 are on the low end of known terrestrial slides. Our compositional survey indicates that outer zones containing hydrated minerals are not anomalous in VM. They are detected in over half of VM landslide outer zones, and half of trough-floor deposits nearby VM outer zones. Observed relationships between landslide morphological parameters and composition suggest that hydrated outer zones may have experienced increased lateral spreading with volume during transport, potentially indicating that basal clays participated in VM landslide emplacement. Though no single analog of VM landslides exists, comparison of our regional morphometric and compositional analysis of VM landslides with aspects of morphologic, compositional, and kinematic examples provides insight into possible mechanisms of transport. Liquefying clay deposits on the trough floor could have feasibly lubricated outer-zone transport. Groundwater percolation or melting of ice/snow warrants further consideration. Near-surface ice or dry fluidization mechanisms could also have played a role in facilitating VM landslide long-distance

transport. It remains for future study to determine their relative importance as compared to that of the prevalent clay minerals discovered in association with landslides here.

Acknowledgements

This project was supported by a National Science Foundation Graduate Research Fellowship (DGE-1144087), Caltech Geological & Planetary Sciences Postdoctoral Fellowship, and GPS Chair's Postdoctoral Fellow & California Alliance for Graduate Education and the Professoriate (NSF AGEP) Postdoctoral Fellow to JAW. Thanks to the MRO-CRISM team for acquisition of several requested images in Valles Marineris and to all spacecraft teams who collected the data used herein. Measurements are included as tables in the manuscript; the graphical data products generated and analyzed during this study are available from the authors upon request.

References

Akers et al. (2012), What caused the landslides in Valles Marineris, Mars? (abs), *Lunar Planet. Sci. XLIII*, 1659.

Al-Shayea, N.A. (2001), The combined effect of clay and moisture content on the behavior of remolded unsaturated soils, *Engineering Geology, 62*, 319-342.

Andrews−Hanna, J. C. and R.J. Phillips (2007), Hydrological modeling of outflow channels and chaos regions on Mars, *J. Geophys. Res., 112*, E08001.

Barnouin-Jha et al. (2005), Comparing landslides to fluidized crater ejecta on Mars, *J. Geophys. Res., 110*, E04010.

Baum et al. (2003), Mechanics of earth flows, In Proceedings of the International Conference FLOWS, Sorrento, Italy.

Bigot-Cormier, F. and D.R. Montgomery (2007), Valles Marineris landslides: Evidence for a strength limit to Martian relief?, *Earth Planet. Sci. Lett., 260*, 179-186.

Bish et al. (2003), Stability of hydrous minerals on the martian surface, *Icarus, 164*, 96-103.

Blasius et al. (1977), Geology of Valles Marineris: First Analysis of Imaging from the Viking 1 Orbiter Primary Mission, *J. Geophys. Res., 82*, 4067-4091.

Brunetti et al. (2014), Analysis of a new geomorphological inventory of landslides in Valles Marineris, Mars, *Earth Planet. Sci. Lett., 405*, 156-168.

Bryn et al. (2005), Explaining the Storegga Slide, *Marine and Petroleum Geology, 22*, 11-19.

Burns, R.G. (1993), Rates and mechanisms of chemical weathering of ferromagnesian silicate minerals on Mars, *Geochimica et Cosmochimica Acta, 57*, 4555-4574.

Carrasco-Núñez et al. (1993), A voluminous avalanche-induced lahar from Citlaltépetl volcano, Mexico: implications for hazard assessment, *J. Volcanology and Geothermal Res., 59*, 35-46.

Christensen et al. (2004), The Thermal Emission Imaging System (THEMIS) for the Mars 2001 Odyssey Mission, *Space Sci. Rev., 110*, 85-130.

Chuang, F.C. and R. Greeley (2000), Large mass movements on Callisto, *J. Geophys. Res., 105*, 20227-20244.

Clark et al. (1990), Material absorption band depth mapping of imaging spectrometer data using a complete band shape least-squares fit with library reference spectra, In Proceedings of the Second Airborne Visible/Infrared Imaging Spectrometer (AVIRIS) Workshop, 2, 4-5.

Clarke, G.K.C. (2005), Subglacial processes, *Annu. Rev. Earth Planet. Sci., 33*, 247–276.

Collins, G.S. and H.J. Melosh (2003), Acoustic fluidization and the extraordinary mobility of sturzstroms, *J. Geophys. Res., 108*, 2473.

Crosta, G. B., Frattini, P., Valbuzzi, E., & De Blasio, F. V. (2018). Introducing a new inventory of large Martian landslides. *Earth and Space Science*, 5(4), 89-119

Davies, T.R. (1982), Spreading of rock avalanche debris by mechanical fluidization, *Rock Mechanics, 15*, 9-24.

De Blasio, F.V. and A. Elverhøi (2008), A model for frictional melt production beneath large rock avalanches, *J. Geophys. Res., 113*, F02014.

De Blasio, F.V. (2011), Landslides in Valles Marineris (Mars): A possible role of basal lubrication by sub-surface ice, *Planet. Space Sci., 59*, 1384-1392.

Di Toro et al. (2004), Friction falls towards zero in quartz rock as slip velocity approaches seismic rates, *Nature, 427*, 436-439.

Dohm et al. (2009), New evidence for a magmatic influence on the origin of Valles Marineris, Mars, *J. Volcanol. Geotherm. Res., 185*, 12-27.

Douglas, R. (2011) Notes on the Portuguese Bend Landslide, Abalone Cove Landslide Abatement District Misc. Report, City of Rancho Palos Verdes.

Dufresne, A. and T.R. Davies (2009), Longitudinal ridges in mass movement deposits, *Geomorphology, 105*, 171-181.

Ehlmann et al. (2011), Subsurface water and clay mineral formation on early Mars, *Nature, 479*, 53-60.

Erismann, T.H. (1979), Mechanisms of large landslides, *Rock Mechanics, 12*, 15-46.

Flahaut et al. (2010), Identification, distribution and possible origins of sulfates in Capri Chasma (Mars), inferred from CRISM data, *J. Geophys. Res., 117*, E11007.

Flahaut et al. (2012), Pristine Noachian crust and key geologic transitions in the lower walls of Valles Marineris: Insights into early igneous processes on Mars, *Icarus, 221*, 420-435.

Forshee, E. J., and Yin, A. (1995), A model for initiation of a mid-Tertiary rock avalanche in the Whipple Mountains area, SE California: Implications for seismicity along low-angle normal faults, *Basin Research*, *7*, 347-350.

Frey-Martínez et al. (2006), Frontally confined versus frontally emergent submarine landslides: A 3D seismic characterization, *Marine and Petroleum Geology*, *23*, 585–604.

Fueten et al. (2005), Structural attitudes of large scale layering in Valles Marineris, Mars, calculated from Mars Orbiter Laser Altimeter data and Mars Orbiter Camera imagery, *Icarus, 175*, 68-77.

Fueten et al. (2008), Stratigraphy and structure of interior layered deposits in west Candor Chasma, Mars, from High Resolution Stereo Camera (HRSC) stereo imagery and derived elevations, *J. Geophys. Res.*, *113*, E10008.

Gourronc et al. (2014), One million cubic kilometers of fossil ice in Valles Marineris: Relicts of a 3.5 Gy old glacial landsystem along the Martian equator, *Geomorphology*, *204*, 235-255.

Haflidason et al. (2005), The dating and morphometry of the Storegga Slide, *Marine and Petroleum Geology*, *22*, 123-156.

Hampton et al. (1996), Submarine landslides, *Reviews of geophysics*, *34*, 33-59.

Harrison, K.P. and M.G. Chapman (2008), Evidence for ponding and catastrophic floods in central Valles Marineris, Mars, *Icarus*, *198*, 351-364.

Harrison, K.P. and R.E. Grimm (2003), Rheological constraints on Martian landslides, *Icarus, 163*, 347-362.

Highland, L.M., and P. Bobrowsky (2008), The landslide handbook—A guide to understanding landslides, U.S. Geological Survey Circular 1325, Reston, Virginia, 129 p.

Howard, K.A. (1973), Avalanche mode of motion- Implications from lunar examples, *Science*,

180, 1052-1055.

Hungr, O. (1995), A model for the runout analysis of rapid flow slides, debris flows, and avalanches, *Can. Geotech. J.*, *32*, 610-623.

Hungr et al. (2014), The Varnes classification of landslide types, an update, *Landslides*, *11*, 167-194.

Hungr, O. and S.G. Evans (2004), Entrainment of debris in rock avalanches: An analysis of a long run-out mechanism, *Geol. Soc. Am. Bull.*, *116*, 1240–1252.

Hsü, K.J. (1975), Catastrophic debris streams (strurzstroms) generated by rockfalls, *Geol. Soc. Am. Bull.*, *86*, 129-140.

Iverson, R.M. (1997), The physics of debris flows, *Reviews of geophysics*, *35*, 245-296.

Iverson, R.M., M.E. Reid, and R.G. LaHusen (1997), Debris-flow mobilization from landslides, *Annu. Rev. Earth Planet. Sci.*, *25*, 85-138.

Iverson et al. (2015), Landslide mobility and hazards: implications of the 2014 Oso disaster, *Earth Planet. Sci. Lett.*, *412*, 197-208.

Johnson, B. (1978), Blackhawk landslide, California, USA, In B. Voigt (ed.) Rockslides and avalanches, 1, pp. 481-504, Elsevier Scientific Publishing Company, Amsterdam.

Johnson, B. C., & Campbell, C. S. (2017). Drop Height and Volume Control the Mobility of Long- Runout Landslides on the Earth and Mars. *Geophysical Research Letters*, 44(24).

Kerr, P.F. and I.M. Drew (1967), Clay mobility, Portuguese Bend, California, *Short Contributions to California Geology*, Special Report 100, 3-16.

Krohn et al. (2014), Mass movement on Vesta at steep scarps and crater rims, *Icarus*, *244*, 120-132.

Kvalstad et al. (2005), The Storegga slide: evaluation of triggering sources and slide mechanics,

Marine and Petroleum Geology, 22, 245-256.

Lajeunesse et al. (2006), New insights on the runout of large landslides in the Valles-Marineris canyons, Mars, *Geophys. Res. Lett., 33*, L04403.

Le Deit et al. (2012), Extensive surface pedogenic alteration of the Martian Noachian crust suggested by plateau phyllosilicates around Valles Marineris, *J. Geophys. Res., 117*, E00J05.

Legros, F. (2002), The mobility of long-runout landslides, *Engineering Geology, 63*, 301-331.

Lowe, D.R. (1975), Water escape structures in coarse-grained sediments, *Sedimentology, 22*, 157-204.

Lucas, A. and A. Mangeney (2007), Mobility and topographic effects for large Valles Marineris landslides on Mars, *Geophys. Res. Lett., 34*, L10201.

Lucas et al. (2011), Influence of the scar geometry on landslide dynamics and deposits: Application to Martian landslides, *J. Geophys. Res., 116*, E10001.

Lucas et al. (2014), Frictional velocity-weakening in landslides on Earth and on other planetary bodies, *Nature Communications, 5*, 3417.

Lucchitta, B.K. (1978), A Large Landslide on Mars, *Geol. Soc. Am. Bull., 89*, 1601-1609.

Lucchitta, B.K. (1979), Landslides in Valles Marineris, Mars, *J. Geophys. Res., 84*, 8097-8113.

Lucchitta, B.K. (1987), Valles Marineris, Mars: Wet Debris Flows and Ground Ice, *Icarus, 72*, 411-429.

Lucchitta et al. (1992), The canyon system on Mars, In H.H. Kieffer, B.M. Jakosky, C.W. Snyder, and M.S. Matthews (eds.), Mars, 1, pp. 453-492, Univ. Arizona Press, Tucson.

Lucchitta et al. (1994), Topography of Valles Marineris: implications for erosional and structural history, *J. Geophys. Res., 99*, 3783–3798.

Lucchitta, B.K. (2010), Lakes in Valles Marineris, In N. Cabrol and E. Grin (eds), Lakes on Mars, pp.111-162, Elsevier, The Netherlands.

Malin, M.C. (1992), Mass movements on Venus: Preliminary results from Magellan cycle 1 Observations, *J. Geophys. Res., 97*, 16337-16352.

Malin et al. (2007), Context Camera Investigation on board the Mars Reconnaissance Orbiter, *J. Geophys. Res., 112*, E05S04.

Mangeney et al. (2010), Erosion and mobility in granular collapse over sloping beds, *J. Geophys. Res., 115*, F03040.

Mazzanti et al. (2016), Inferring the high velocity of landslides in Valles Marineris on Mars from morphological analysis, *Earth, Planets and Space, 68*, 1-16.

McEwen, A.S. (1989), Mobility of large rock avalanches: Evidence from Valles Marineris, Mars, *Geology, 17*, 1111-1114.

McEwen et al. (2007), Mars Reconnaissance Orbiter's High Resolution Imaging Science Experiment (HiRISE), *J. Geophys. Res., 112*, E05S02.

McSaveney, M.J. (1978), Sherman Glacier rock avalanche, Alaska, USA, In: Voight, B. (ed.), Rockslides and Avalanches 1, Dev. Geotech. Eng., 14A, S. 197-258.

Mège, D. and O. Bourgeois (2010), Equatorial glaciations on Mars revealed by gravitational collapse of Valles Marineris wallslopes, *Earth Planet. Sci. Lett., 310*, 182-191.

Mège, D. and P. Masson (1996), Amounts of crustal stretching in Valles Marineris, Mars, *Planet. Space Sci., 44*, 749-782.

Melosh, H.J. (1979), Acoustic fluidization- A new geologic process, *J. Geophys. Res., 84*, 7513-7520.

Melosh, H.J. (1987), The mechanics of large rock avalanches, *Reviews in Engineering Geology,*

7, 41-50.

Metz et al. (2010), Thin-skinned deformation of sedimentary rocks in Valles Marineris, Mars, *J. Geophys. Res., 115*, E11004.

Morrow, C.A., D.E. Moore, and D.A. Lockner (2000), The effect of mineral bond strength and adsorbed water on fault gouge frictional strength, *Geophys. Res. Lett., 27*, 815-818.

Murchie et al. (2007), Compact Reconnaissance Imaging Spectrometer for Mars (CRISM) on Mars Reconnaissance Orbiter (MRO), *J. Geophys. Res., 112*, E05S03.

Murchie et al. (2009a), A synthesis of Martian aqueous mineralogy after 1 Mars year of observations from the Mars Reconnaissance Orbiter, *J. Geophys. Res., 114*, E2.

Murchie et al. (2009b), Compact Reconnaissance Imaging Spectrometer for Mars investigation and data set from the Mars Reconnaissance Orbiter's primary science phase, *J. Geophys. Res., 114*, E00D07.

Mustard et al. (2008), Hydrated silicate minerals on Mars observed by the Mars Reconnaissance Orbiter CRISM instrument, *Nature*, *454*, 305-309.

Nedell et al. (1987), Origin and evolution of the layered deposits in the Valles Marineris, Mars, *Icarus, 70*, 409-441.

Neukum, G. and R. Jaumann (2004), The High Resolution Stereo Camera of Mars Express, In (eds.) A. Wilson and A. Chicarro, Mars Express: The Scientific Payload, pp. 17-35, ESA SP-1240, Noordwijk, The Netherlands.

Niles, P.B. and J. Michalski (2009), Meridiani Planum sediments on Mars formed through weathering in massive ice deposits, *Nature Geoscience, 2*, 215-220.

Pelkey et al. (2007), CRISM multispectral summary products: Parameterizing mineral diversity on Mars from reflectance, *J. Geophys. Res., 112*, E08S14.

Peulvast et al. (2001), Morphology, evolution and tectonics of Valles Marineris wall slopes (Mars), *Geomorphology, 37*, 329-352.

Peulvast, J.P. and P.L. Masson (1993), Erosion and tectonics in central Valles Marineris (Mars): A new morpho-structural model, *Earth, Moon, and Planets, 61*, 191-217.

Quantin et al. (2004a), Morphology and geometry of Valles Marineris landslides, *Planet. Space Sci., 52* , 1011-1022.

Quantin et al. (2004b), Ages of Valles Marineris (Mars) landslides and implications for canyon history, *Icarus, 172*, 555-572.

Roach et al. (2010), Hydrated mineral stratigraphy of Ius Chasma, Valles Marineris, *Icarus, 206*, 253-268.

Roche et al. (2011), On the run-out distance of geophysical gravitational flows: Insight from fluidized granular collapse experiments, *Earth Planet. Sci. Lett., 311*, 375-385.

Schenk, P.M. and M.H. Bulmer (1998), Origin of mountains on Io by thrust faulting and large-scale mass movements, *Science, 279*, 1514-1517.

Schultz, R.A. (1998), Multiple-process origin of Valles Marineris basins and troughs, Mars, *Planet. Space Sci., 46*, 827-829.

Schultz, R.A. (2002), Stability of rock slopes in Valles Marineris, Mars, *Geophys. Res. Lett, 29*, 1932.

Schultz et al. (2010), Interpretation and analysis of planetary structures, *J. Structural Geol., 32*, 855-875.

Shaller, P.J. (1991), Analysis and implications of large Martian and terrestrial landslides, Ph.D. Thesis, pp.586, Calif. Inst. Tech., Pasadena, California.

Shingareva, T.V. and R.O. Kuzmin (2001), Mass-wasting processes on the surface of Phobos,

Solar System Research, 35, 431-443.

Shreve, R. L. (1966), Sherman landslide, Alaska, *Science, 154*, 1639-1643.

Shreve, R. L. (1968a), Leakage and fluidization in air-layer lubricated avalanches, *Geol. Soc. Am. Bull., 79*, 653-658.

Shreve, R. L. (1968b), The Blackhawk landslide, *Geol. Soc. Am. Special Papers, 108*, 1-48.

Singer et al. (2012), Massive ice avalanches on Iapetus mobilized by friction reduction during flash heating, *Nature Geoscience, 5*, 574-578.

Soukhovitskaya, V. and M. Manga (2006), Martian landslides in Valles Marineris: Wet or dry?, *Icarus, 180*, 348-352.

Thollot et al. (2012), Most Mars minerals in a nutshell: Various alteration phases formed in a single environment in Noctis Labyrinthus, *J. Geophys. Res.,117*, E11.

Vaniman et al. (2014), Mineralogy of a mudstone at Yellowknife Bay, Gale crater, Mars, *Science, 343*.

Viviano-Beck, C.E. and S.L. Murchie (2014), Hydrothermally altered stratigraphy in the walls of Valles Marineris (abs), *Lunar Planet. Sci. XLV*, 1963.

Warner et al. (2013), Fill and spill of giant lakes in the eastern Valles Marineris region of Mars, *Geology, 41*, 675-678.

Watkins et al. (2015), Long-runout landslides and the long-lasting effects of early water activity on Mars, *Geology, 43*, 107-110.

Watry, S.M. and P.L. Ehlig (1995), Effect of test method and procedure on measurements of residual shear strength of bentonite from the Portuguese Bend landslide, *Reviews in Engineering Geology, 10*, 13-38.

Weidinger, J.T. and O. Korup (2009), Frictionite as evidence for a large Late Quaternary

rockslide near Kanchenjunga, Sikkim Himalayas, India- Implications for extreme events in mountain relief destruction, *Geomorphology, 103*, 57-65.

Weiss, D.K. and J.W. Head (2014), Ejecta mobility of layered ejecta craters on Mars: Assessing the influence of snow and ice deposits, *Icarus, 233*, 131-146.

Weitz et al. (2011), Diverse mineralogies in two troughs of Noctis Labyrinthus, Mars, *Geology, 39*, 899-902.

Weitz et al. (2012), Geologic relationships between gray hematite, sulfates, and clays in Capri Chasma, *J. Geophys. Res., 117*, E00J09.

Weitz et al. (2014), Fresh exposures of hydrous Fe‐bearing amorphous silicates on Mars, *Geophys. Res. Lett., 41*, 8744-8751.

Weitz et al. (2015), Mixtures of clays and sulfates within deposits in western Melas Chasma, Mars, *Icarus, 251*, 291-314.

Williams, R.M. and C.M. Weitz (2014), Reconstructing the aqueous history within the southwestern Melas basin, Mars: Clues from stratigraphic and morphometric analyses of fans, *Icarus, 242*, 19-37.

Witbeck et al. (1991), Geologic map of the Valles Marineris region, Mars, scale 1:2000000, U.S. Geol. Survey Misc. Inv. Series Map I-2010.

Yin, A. (2012a), An episodic slab-rollback model for the origin of the Tharsis rise on Mars: Implications for initiation of local plate subduction and final unification of a kinematically linked global plate-tectonic network on Earth, *Lithosphere, 4*, 553-593.

Yin, A. (2012b), Structural analysis of the Valles Marineris fault zone: Possible evidence for large-scale strike-slip faulting on Mars, *Lithosphere, 4*, 286-330.

Zuber et al. (1992), The Mars Observer Laser Altimeter Investigation, *J. Geophys. Res., 97*,

7781-7797.